

Chapter 4

Cavity Ignition in Supersonic Flows



Scramjets are promising propulsion systems for hypersonic flight vehicles. Development of scramjets relies on sufficient understanding of the complex mixing, ignition and combustion processes inside a scramjet combustor. Current scramjets usually require flame holding devices which provide subsonic environments to facilitate flame ignition and stabilization, because the ignition delay time of hydrocarbon fuels is long relative to their residence time in the combustor. The most common flame holding device is a cavity with a slanted rear wall. This flame holder scheme is generally combined with transverse injection in supersonic combustors.

The ignition process in supersonic flows is complicated, and depends on many factors such as the local fuel equivalence ratio, the flame holder configuration, the fuel auto-ignition ability, the ignition energy and the flow conditions near the ignition location. For cavity-based supersonic combustors, a major concern regarding the ignition is how to establish stable subsonic combustion regions around and inside cavities, which motivates researches on chemical and physical phenomena on cavity ignition. This chapter introduces our studies through four aspects, involving diverse ignition methods, flame behaviours during ignition, ignition mechanisms and auto-ignition effects.

4.1 Ignition Processes Under Different Ignition Methods

Interactions between turbulence and chemical reactions are vital for ignition process. In cavity-based scramjet combustors, the core flow of supersonic inflows usually has a velocity of 1000 m/s, and the velocity of the recirculating flow inside cavities often varies from 0 to 200 m/s. The core flow and the shear layer over cavities trigger strong turbulent dissipation which challenges the initial flame propagation, although cavities provide an ignition-friendly environment. Therefore, the cavity ignition process presents many unique characteristics. These characteristics may even change as different ignition methods are used, which is not fully understood

yet. This section sketches typical ignition processes with respect to diverse ignition methods.

4.1.1 Spark Ignition

Among many methods for cavity ignition, spark ignition is still the most widely used. The main shortage for spark ignition is the low ignition energy. Spark ignition is often used to ignite cavity-based scramjets that utilize hydrogen or gaseous hydrocarbons as fuels. For liquid kerosene that requires larger ignition energy, however, employing spark ignition without aid of other methods is less reported.

Figures 4.1 and 4.2 demonstrate a typical spark ignition process via high-speed imaging and schlieren in a direct-connected test facility fueled by hydrogen [1]. The inflow conditions were $Ma = 1.92$ with stagnation state $T_0 = 846$ K and $P_0 = 0.7$ MPa. As shown in Fig. 4.1, the initial flame kernel induced by spark appears around the igniter which is near to the front wall of the cavity. The injection valve opens at $t = 0.0$ ms, and simultaneously the spark plug in the upper cavity is triggered. The spark brightness is identified in Fig. 4.1b and c with white circles. Before $t = 0.5$ ms the initial flame kernel grows slow, but the flame propagation suddenly speeds up, as shown in images of $t = 0.5$ ms and $t = 0.75$ ms. In this short period, the flame speed approximately reaches 400 m/s. A reasonable explanation for this high flame speed is that the flame kernel penetrates the cavity shear layer and ignites the fuel in the shear layer, and the high-speed shear layer transfers flame

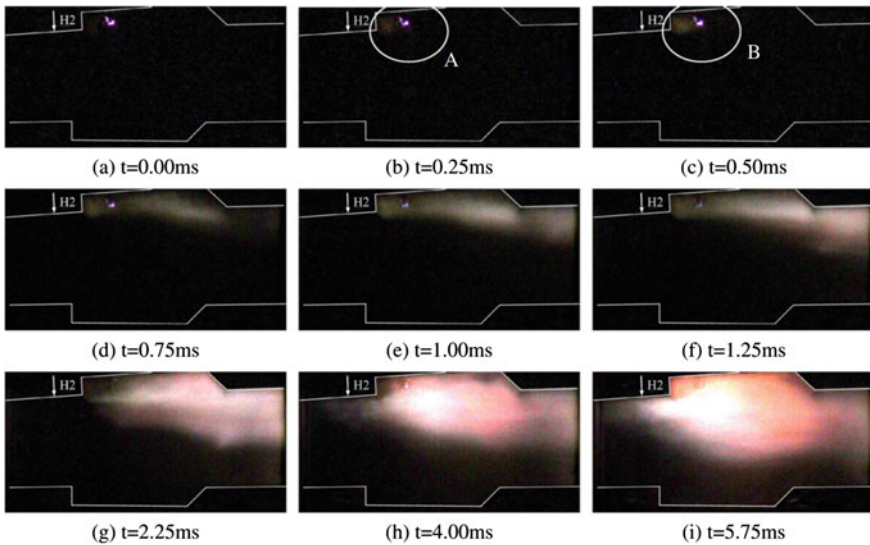


Fig. 4.1 High-speed images of spark ignition process of hydrogen [1]

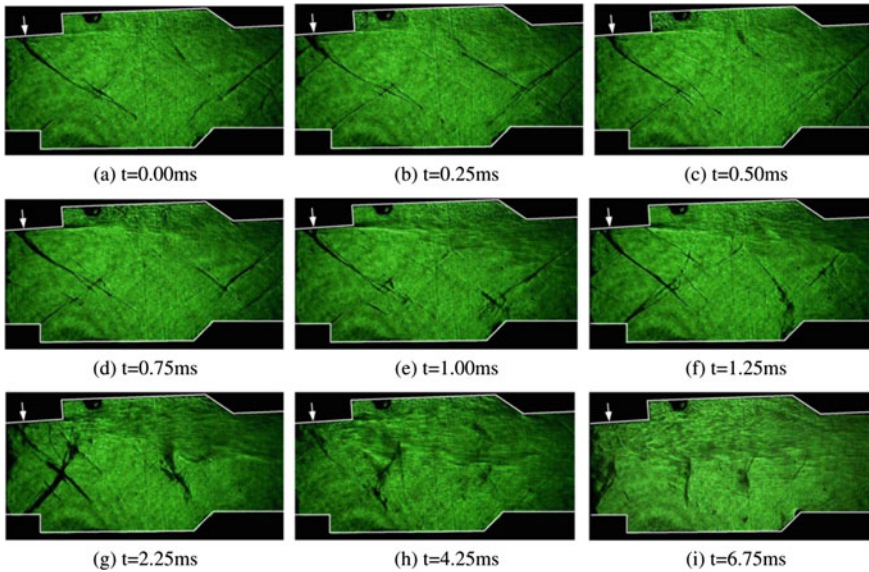


Fig. 4.2 High-speed schlieren images of spark ignition process of hydrogen around the T2 cavity with T2 ignition [1]

downstream very quickly. Images of $t = 0.75$ ms to $t = 2.25$ ms show that after the fuel downstream of the upper cavity being ignited, the flame propagates upstream due to the pressure increase caused by heat release. Meanwhile, the flame spreads transversely, igniting the fuel in the core flow. During this period, the flame appears distortion which might result from shockwave incidence from the bottom cavity. At $t = 4.00$ ms, the flame begins stabilizing and the flame front extends to the injection location.

Schlieren images during the ignition process are shown in Fig. 4.2. Figures 4.1 and 4.2 are from two individual ignition experiments whose operating conditions are identical. In Fig. 4.2 the cavity shear layer and heat release region can be recognized clearly. The shock trains and flame bounds change hugely owing to unsteadiness of the ignition process.

4.1.2 Piloted Ignition

Piloted ignition is widely applied in practical scramjets in which utilizing spark ignition only is unable to achieve reliable ignition, for example when the fuel is kerosene. Piloted ignition refers to establishing initial combustion with the help of pilot flame which is formed by igniting chemically active fuels, such as hydrogen and ethylene. In piloted ignition, the spray usually starts as immediately as the pilot flame is established. Thus the spray and the pilot injection coexist for a short period. The pilot injection terminates once the spray flame is stabilized.

Compared with direct spark ignition in the cavity, piloted ignition could broaden ignitable conditions. This is because the pilot flame not only supplies vast heat and active radicals, but also induces pre-combustion shock trains upstream of the cavity, which enhances mixing of the spray and the core flow. The mixing enhancement pertaining to the precombustion shock trains was observed in Ref. [2] which experimentally investigated the ignition transition phase in model supersonic combustor. In the experiment three types of ignition processes were compared: spark ignition of ethylene, spark ignition of kerosene, and piloted ignition with kerosene as the spray fuel and ethylene as the pilot fuel.

The left column of Fig. 4.3 records the density field variation around the cavity, and the right column corresponds to a region in the isolator upstream of the cavity. The leading junction of the shock train is tracked from the left column to the right column, as indicated by the time steps. Ethylene is transversely injected from the location denoted by the arrow, under a injection pressure of 2 MPa. The fuel trace and the bow shock are clear in the image of $t = 0$ ms. There exist irremovable reflected shockwaves in the isolator, which are attributed to small gaps between different sections. But those shockwaves are too weak to affect the bulk velocity of supersonic primary flow. Following the spark at $t = 0$ ms, the first shockwave intersection appears at $t = 3.5$ ms, and then it is pushed upstream to the isolator, as

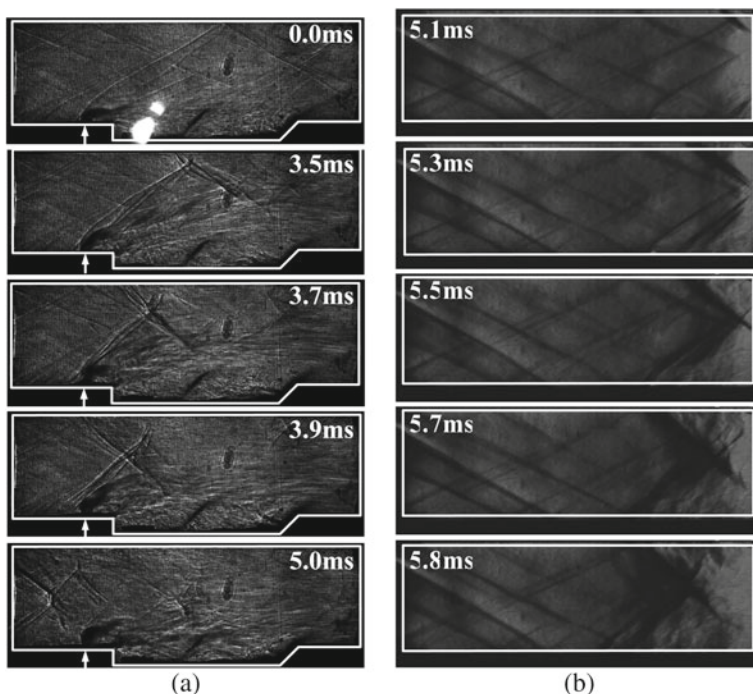


Fig. 4.3 Schlieren images showing evolution of precombustion shock train during spark ignition of ethylene [2]

shown in the right column. The speed at which the shockwave intersection moves upstream is estimated to be 50–100 m/s, according to the camera's frame rate. This speed is close to the flame propagation speed in conditions of high temperature and turbulence, but much less than the detonation speed (1 km/s or above). The moving of shockwave intersection is caused by separation of boundary layers on walls, and this separation results from local heat release. It is then conclude that the initial flame development is a subsonic flame propagation dominated by expansion of the cavity flame.

Figure 4.4 reports the density field change in the isolator during piloted ignition. The camera setup is similar to that used in Fig. 4.3a. At $t = 0$ ms, the leading shockwave induced by the cavity flame has reached the right side. Nevertheless, the leading shockwave is pushed down when the fuel touched the downstream ethylene flame owing to heat-absorbing effect of cold fuel droplets. At $t = 1.8$ ms, the kerosene flame first appears. From images of $t = 1.8$ ms to 3.2 ms, the effect of the precombustion shock train on the spray can be clearly observed. The spray lifts and the fuel evaporates immediately when swept by the leading shockwave, which enhances the mixing and combustion processes. This effect is also verified by the experimental

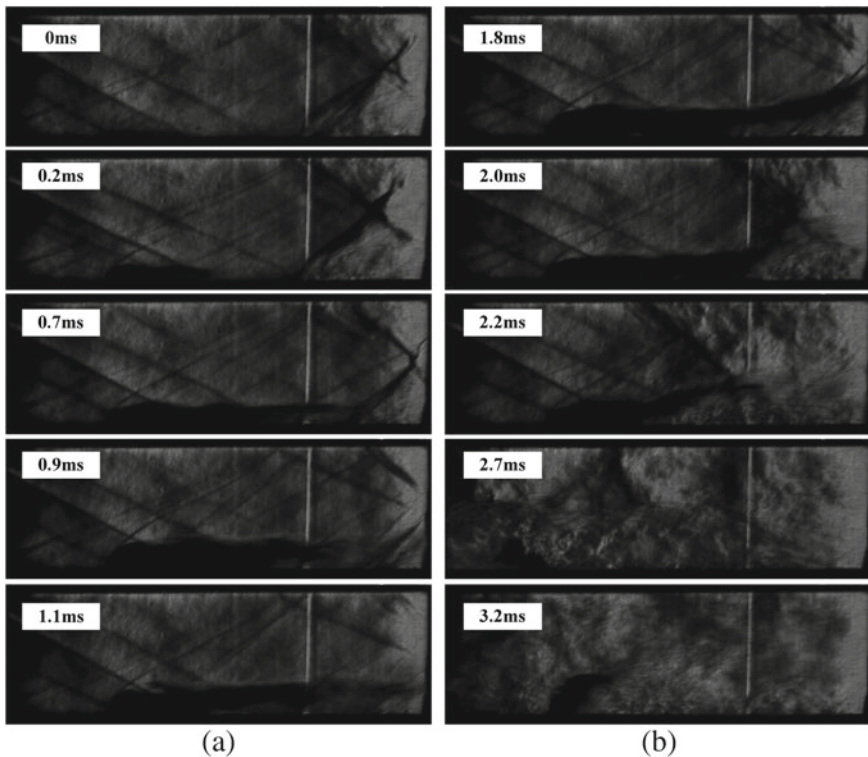


Fig. 4.4 Schlieren images showing evolution of piloted ignition with kerosene as the spray fuel and ethylene as the pilot fuel [2]

cases that a weak flame without a generated shock train cannot lead to a successful piloted ignition event [2].

4.1.3 *Gliding-Arc-Discharge (GAD) Ignition*

For the spark ignition discussed in Sect. 4.1.1, the discharge produces thermal equilibrium plasmas so that the ignition is caused by heating of fuel-oxidizer mixture in a small-volume around the arc channel. In recent decades, nevertheless, utilizing non-equilibrium plasmas for ignition has gained increasing interest. Non-equilibrium plasmas could effectively generate active radicals substantially reducing the ignition delay time, which greatly facilitates combustion organization in scramjet engines.

GAD refers to plasmas generated between separated electrodes in a fast gas flow. The gliding arc is stretched in the flow field, changing from the equilibrium state to the non-equilibrium state. In the non-equilibrium state, up to 70–80% of the gliding arc power is dissipated, which means that the GAD has the potential to efficiently stimulate nonequilibrium chemical reactions significant for the ignition process.

Figure 4.5 illustrates a typical ignition process using the GAD [3]. The experiment was implemented in a cavity-based scramjet combustor. The inflow had a stagnation temperature of 1600 K and a stagnation pressure of 1.65 MPa. The GAD power supply had an average power of 2 kW and a maximum peak voltage of 20 kV.

In Fig. 4.5 multiple flame kernels first appear but are then blown off, from $t = -8075 \mu\text{s}$ to $t = -8025 \mu\text{s}$. At $t = 0 \mu\text{s}$, a flame kernel appears again and

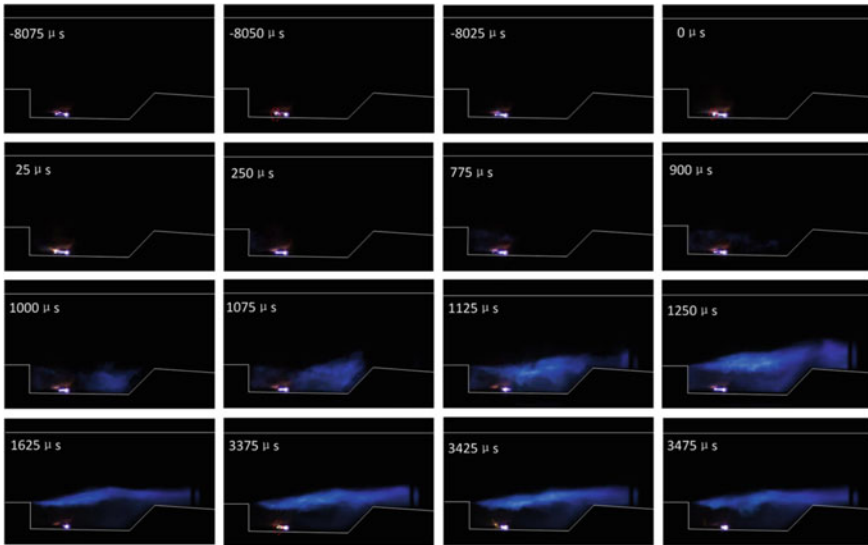


Fig. 4.5 High-speed images for gliding-arc-discharge ignition [3]

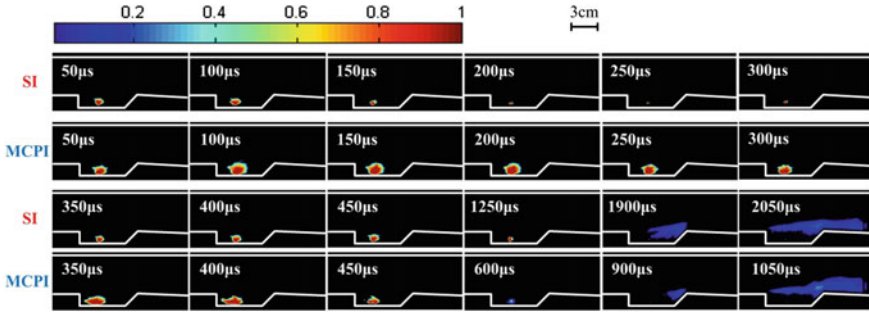


Fig. 4.6 Comparison of CH* chemiluminescence images related to spark ignition and multichannel plasma igniter [4]

then successfully spreads. The flame kernel is wrinkled anti-clockwise which agrees with the flow pattern inside the recirculation zone. The flame further propagates, filling the cavity at $t = 1075 \mu\text{s}$. Then the fuel in the cavity shear layer is ignited at $t = 1125 \mu\text{s}$, following that flame in the cavity begins to dissipate at $t = 1250 \mu\text{s}$. Finally, the flame stabilizes at $t = 1625 \mu\text{s}$. During the whole ignition process, the GAD continuously induces flame kernels inside the recirculation zone, which speeds up the ignition process. It costs 131 ms to form a stabilized flame from the discharge beginning.

It is experimentally observed that the GAD triggers initial flame kernels when it reaches the maximum length. This phenomenon is consistent with the state transition and energy dissipation of GAD. As above mentioned, the GAD in non-equilibrium state could generate active radicals helpful for formation of initial flame kernels. Also, the instantaneous power of GAD increases as the arc is continuously stretched, according to the voltage and current records during the ignition process.

A relatively large kernel can be realized by utilizing multi-channel plasma igniter (MCPI) powered by a conventional ignition power supply [4]. Fig. 4.6 compares the flame kernel developments of spark ignition (SI) and MCPI in a scramjet combustor with inflow conditions of $Ma = 2.52$, stagnation pressure $P_0 = 1.6 \text{ MPa}$ and stagnation pressure $T_0 = 1600 \text{ K}$. Figure 4.6 shows that the flame kernel of MCPI is much larger than that of SI. For MCPI the flame takes $900 \mu\text{s}$ to fill the cavity and reach the shear layer, but for SI the time is $1000\text{-}\mu\text{s}$ longer.

4.1.4 Laser-Induced Plasma (LIP) Ignition

Ignition through LIP can be classified as laser thermal ignition, laser-induced photochemical ignition, laser-induced resonant breakdown ignition, and laser-induced spark ignition [5]. Non-resonant breakdown is the most common, because it does not require a wavelength to photo-dissociate particular target species. Compared with ignition methods based on electrical discharge, LIP ignition can precisely control

the rate and amount of energy decomposition, and flexibly modify the ignition position. Through synchronizing the laser and advanced optical diagnostic systems, the instantaneous ignition process could be investigated intensively in the time scale of nanoseconds (or even picoseconds), which is fascinating for ignition studies in a supersonic flow. Disadvantages of LIP ignition chiefly include complication and incompactness of laser systems, necessity to design optical paths for laser beams, and impossibility to provide uniform energy decomposition in a relatively large volume.

Figure 4.7 shows the LIP ignition process in a cavity-based supersonic combustor with ethylene as the fuel [6]. The inflow's Mach number is 2.1, the stagnation temperature is 947 K and the total pressure is 0.65 MPa. A 1064-nm laser beam, which came from a Q-switched Nd:YAG laser source running at 10 Hz and had 940 mJ



Fig. 4.7 High-speed images for evolution of the flame kernel induced by LIP ignition [6]

per pulse, was focused into the cavity for ignition. The laser was directed into the upstream cavity at $t = 0 \mu\text{s}$.

The image of $t = 50 \mu\text{s}$ in Fig. 4.7 shows a bright and white light emitted in the bremsstrahlung process of LIP. The ionized plasma is almost round at the start, but then wrinkles due to the turbulence, as shown in the image of $t = 100 \mu\text{s}$. The yellow light arises, because the combustion chain reactions are initiated and the flame kernel is formed. From $t = 275 \mu\text{s}$ to $375 \mu\text{s}$, the top of the flame kernel is entrained into the cavity shear layer, and then quenches out due to the high strain rate. The left flame kernel rotates anti-clockwise owing to the entrainment of circulation zone inside cavity. The flame kernel reaches to the front wall at $t = 725 \mu\text{s}$ and is stabilized at the corner for about $200 \mu\text{s}$. At $t = 925 \mu\text{s}$, the flame begins to spread downstream in the cavity via the bottom of the shear layer. Then the flame fully fills the cavity at $t = 1950 \mu\text{s}$. When the shear layer impinges on the cavity ramp, the burning combustible mixture in cavity shear layer is transported into the core flow, following that the cavity shear layer stabilized flame is formed. The images of $t = 2300 \mu\text{s}$ to $t = 2950 \mu\text{s}$ further show the establishment of stabilized flame in the cavity downstream.

Ignition process by two-pulse laser-induced plasma is shown in Fig. 4.8 [7]. In the experiment, the second laser pulse was triggered $200 \mu\text{s}$ after the first one. This $200\text{-}\mu\text{s}$ delay approximately equals to the time in which the flame kernel produced by the first laser pulse was transported to the cavity corner. Note that the flame structures

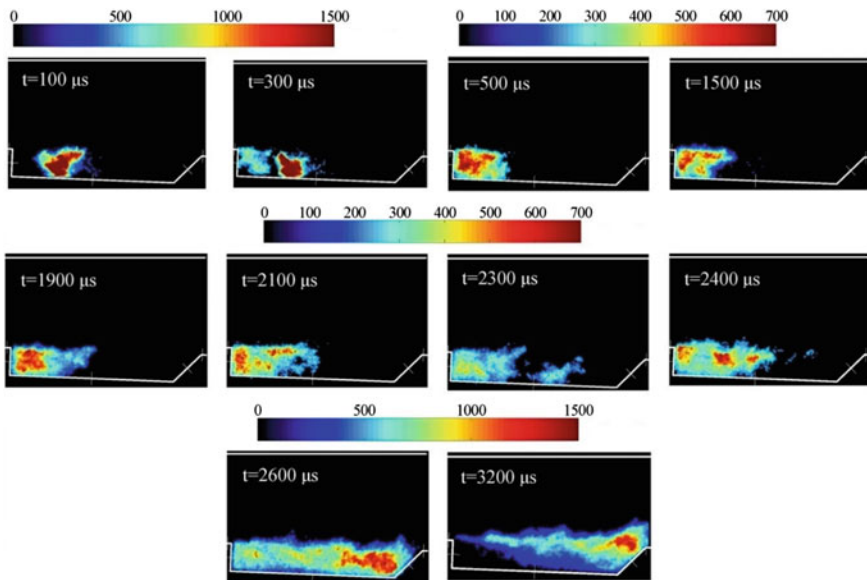


Fig. 4.8 Instantaneous distribution of OH^* chemiluminescence during ignition by dual-laser laser-induced plasma [7]

represented by OH* chemiluminescence were obtained from different test runs, due to low frame rate of the used ICCD camera.

The ignition process resembles that using a single laser pulse. The main difference is that the two laser pulses are combined to form the initial flame kernel. As reported in Fig. 4.8, the two kernels merge together at $t = 500 \mu\text{s}$. The flame kernel triggered by the second laser pulse is weaker than that by the first one, because the first pulse improves the temperature and reduces the flow density in the laser focus, decreasing the absorbed energy of the second pulse. From $t = 500 \mu\text{s}$ to $1900 \mu\text{s}$, the flame in the recirculation zone then enters into a quasi-stable state. Further, the flame spreads downstream to fill the whole cavity from $t = 1900 \mu\text{s}$ to $2600 \mu\text{s}$. Finally, the flame is stabilized along the shear layer over the cavity, as shown in the image of $t = 3200$.

4.2 Flame Behaviors During Ignition

Since the ignition process is affected by many factors and partially stochastic, the flame usually behaves differently from one ignition event to another, even with identical configurations. The flame behaviors during ignition directly determine ignition results and closely correlate to the ignition mechanism. In this section, studies of flame behaviors during processes of the flame kernel formation and the initial flame propagation are introduced accordingly.

4.2.1 *Experimental and Numerical Setups*

The studies about the flame kernel formation and the initial flame propagation are based on different setups. During the flame kernel formation, flame behaviors are investigated in a single-cavity supersonic combustor ignited by LIP, since the rate, amount and position of ignition energy injection can be altered flexibly. During the initial flame propagation, nonetheless, flame behaviors are studied in a single-cavity combustor and a multi-cavity one, both with the spark ignition. Configuration used in these studies are outlined in this section for reference.

4.2.1.1 LIP Ignition in a Single-Cavity Supersonic Combustor

A direct-connected test facility composed of an air heater, a supersonic nozzle and a scramjet model combustor was used for experiment. Through the air heater burning pure ethanol and oxygen, the air at a mass flow rate of 1 kg/s was continuously heated to a stagnation temperature of $T_0 = 1650 \text{ K}$ and a stagnation pressure of $P_0 = 2.6 \text{ MPa}$. The mole fraction of oxygen in the vitiated air was 21%. The outlet of air heater was equipped with a two-dimensional Larval-nozzle to accelerate the heated air to $Ma = 2.92$.

Shown in Fig. 4.9 is the model scramjet engine. A constant-area 315 mm long isolator with height of 40 mm and width of 50 mm was directly connected to the exit of nozzle, followed by a 512-mm-long combustor whose lower wall diverges at an angle of 2.25°. A 220 mm long expansion section with a single-side expansion angle of 3° was at the end of the combustor. One cavity was installed on the lower wall.

As illustrated in Fig. 4.10, the cavity depth $D = 15$ mm, cavity length to depth ratio $L/D = 7$, and the aft ramp angle was 45°. Ethylene at room temperature was injected through 2-mm-diameter orifice at 10-mm upstream of the leading edge along the central plane. The injection pressure of ethylene before was 2.5 MPa. The overall equivalent ratio was kept at 0.152 for all the tests. A Q-switched Nd:YAG laser system (Vlite-500) was used for ignition. The laser system provided 532 nm laser pulses with a 10-ns width, a 12-mm diameter and 350-mJ maximum pulse energy. Nonetheless, only 85% of the laser pulse energy passed through the lens and the quartz window of the combustor. The laser pulses were focused by a convex lens ($f = 150$ mm) to produce the plasma for ignition. The breakdown region denoted by red spots had a cone shape. The shape size given in the figure was estimated when the laser pulse energy approximately equalled 300 mJ. There existed three different ignition positions that all of them located in the central plane, with a 5-mm distance above the cavity bottom. Along the streamwise direction, their distances to the front wall of the cavity were 22.5 mm, 45.0 mm and 67.5 mm, respectively. Hereafter, the three positions are separately referred to as “P1”, “P2” and “P3”.

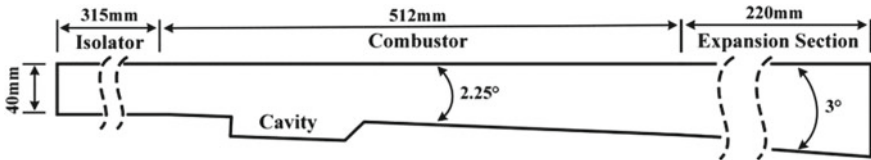
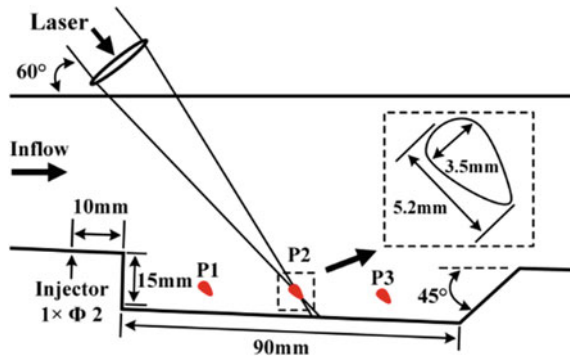


Fig. 4.9 Schematic of the model scramjet engine and the cavity [8]

Fig. 4.10 Schematic of the cavity and the optical configuration [8]



For the purpose of marking flame locations, CH^* and OH^* chemiluminescence were captured simultaneously. The CH^* chemiluminescence was recorded by a high-speed camera (Photron SA-Z) with a Nikon 85 mm f/1.8 lens and a bandpass filter (centered at 430 nm, with a 10 nm FWHM). The frame rate of the camera was set at 25,000 frames per second (fps) with an exposure time of 40 μs , and the spatial resolution was 240- μm per pixel. An intensified charge-coupled device (ICCD) camera equipped with a UV lens (95 mm focal length and f/4.1) and a bandpass filter (centered at 311 nm, with a 10-nm FWHM) was applied to acquire OH^* chemiluminescence. The ICCD camera operated at 3 fps with a shutter time of 2 μs , with a spatial resolution of 250- μm per pixel. As the cameras were mounted on the same side, neither of them oriented normal to test section precisely. The consequent image distortion was then corrected by an image processing program.

4.2.1.2 Spark Ignition in a Single-Cavity Supersonic Combustor

Main components of the direct-connected test facility and their functions have been given in the last section, and in this section only the differences are mentioned. As shown in Fig. 4.11, The cavity flame-holder along was mounted on the bottom wall which had an expansion angle of 1° . The plug was located in the middle of the cavity. The impulse excitation energy of the plug was 5.0 J and the excitation frequency was 50 Hz [9]. A quartz window with a 162-mm length and a 38-mm width was embedded into the top wall of the combustor. Meanwhile another four quartz windows with a 148-mm length and a 90-mm width were embedded into the side walls of the combustor, as plotted in Fig. 4.12. The cavity bottom length L and aft ramp angle A were 80 mm and 45° respectively. The model scramjet combustor width was 50 mm. The cavity bottom length L and aft ramp angle A were respectively 80 mm and 45° . The model scramjet combustor had a width of 50 mm. As the leading edge height $D1$ of 20 mm is taller than the rear wall height $D2$ of 16 mm, this kind of cavity is often called the real-wall-expansion cavity [10–13].

The experiment involved three cavity geometries A, B and C with rear wall heights of 16 mm, 12 mm and 8 mm, respectively. Two groups of porthole injectors, represented by red spots in Fig. 4.12, were located 10-mm and 30-mm upstream of the front wall of the cavity, separately. Each group consisted of three injectors evenly spaced along the spanwise direction.

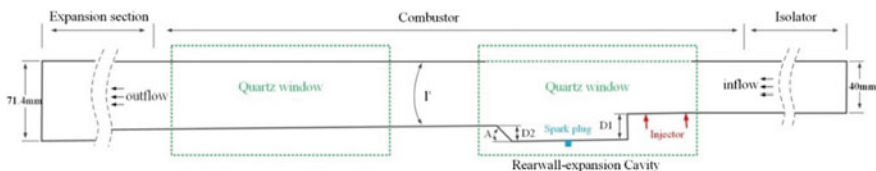


Fig. 4.11 Schematic of the scramjet engine and the cavity [12]

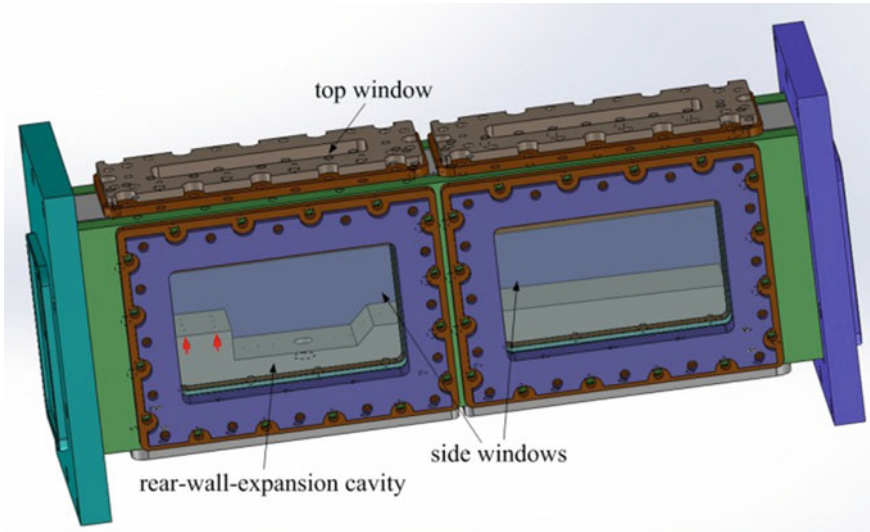


Fig. 4.12 Rear-wall-expansion cavity combustor [14]

The ignition and flame propagation were visualized by two high-speed cameras, one camera capturing flame chemiluminescence from the side view while the other from the top view. The cameras worked at 20,000 fps with a shutter time of $1/20683$ s and an aperture number of 1.4. The pressure along the combustor's bottom wall was recorded by 32 static pressure taps in a sample frequency of 100 Hz with $\pm 0.5\%$ uncertainties.

4.2.1.3 Spark Ignition in a Multi-cavity Supersonic Combustor

Figure 4.13 shows the two cavity configurations adopted in the direct-connected test facility. Flame was observed through the glass windows embedded in the side wall, by a high-speed camera with an imaging frequency of 5,000 fps and an exposure time of $1/6$ ms. In the parallel dual-cavity configuration, two cavities were oppositely installed on the top and bottom walls. Nevertheless, the tandem dual-cavity configuration adopted two cavities which adjoined along the streamwise direction. Sharing the same size, all the cavities had a cavity depth of 8 mm, a length-to-depth ratio of 7 and an rear wall angle of 45° . Hydrogen injectors were located in the central plane with a 10-mm distance upstream of the leading edges. Each injector exit had a diameter of 2 mm. It is noticed that there were two injectors for the parallel dual-cavity configuration but only one for the tandem dual-cavity configuration. The injection pressure in the former configuration was twice that in the latter, in order to keep the same global equivalence ratio.

The combustion processes corresponding to the two configurations were also numerical investigated. Figure 4.14 plots the xy -plane projection of the combustor

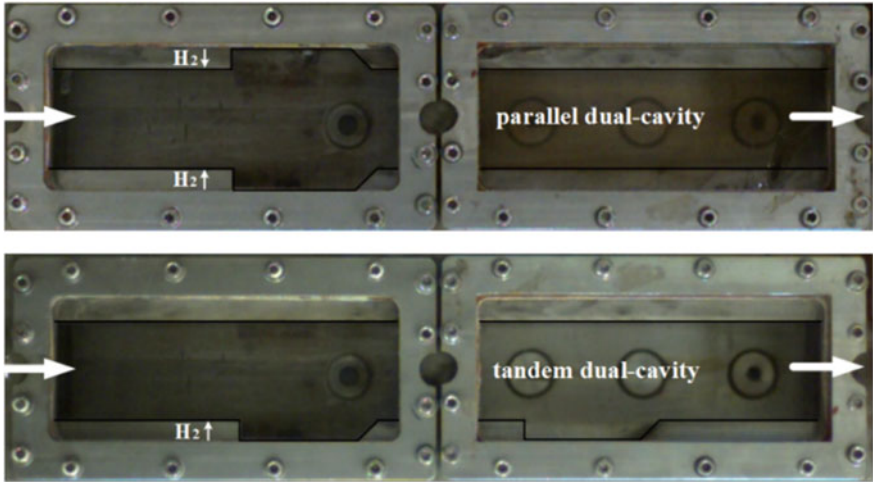


Fig. 4.13 Supersonic combustors with tandem and parallel dual-cavity [15]

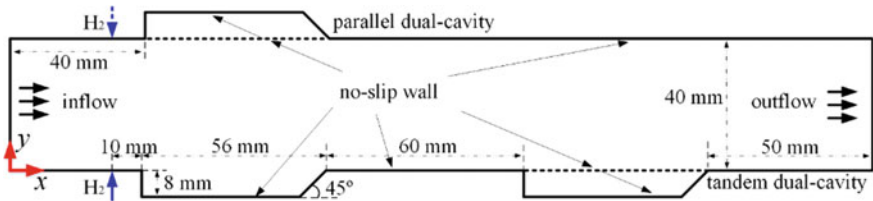


Fig. 4.14 Schematic of computational domain of dual-cavity combustor [15]

in the simulation with key sizes. Along the z -axis the size of the combustor was 25 mm. The total grid points were about 10.3 million and 11.5 million for the parallel dual-cavity and the tandem dual-cavity configurations, respectively. In focused computational region, the grid had a resolution of $\Delta x^+ \approx 1-50$, $\Delta y^+ \approx 1-30$ and $\Delta z^+ \approx 20-50$, on basis of the wall stress τ_w at the inlet bottom floor. It may be coarse for a wall-resolved LES, but is suitable for a hybrid approach. The inflow boundary layers on the top and bottom walls had a thickness of 3 mm, which aimed to simulate the flow condition at the isolator exit in experiments.

In the simulation, the fifth-order Weighted Essentially Non-Oscillatory (WENO) scheme [16] was adopted for inviscid fluxes, and viscous fluxes were calculated by the 2nd-order central scheme. Temporal integration was performed by a second-order dual time-step approach, with the inner iteration achieved by a lower-upper symmetric Gauss-Seidel (LU-SGS) method. The Spalart-Allmaras Reynolds-Averaged Navier-Stokes (RANS) model and the Yoshizawa sub-grid scale (SGS) model were blended in the hybrid RANS/LES method. One equation S-A RANS model and one equation Yoshizawa SGS model for LES were used in near-wall regions and the regions away from the solid wall, respectively. The turbulence modelling process

Table 4.1 Experiment and simulation condition

	Ma	T_0 / K	P_0 / MPa	Y_{O_2}	Y_{H_2O}	Y_{N_2} and Y_{CO_2}	Y_{H_2}
Air inflow	2.52	1486	1.6	0.2338	0.0622	0.704	0.0
Hydrogen jet	1.0	300	0.63, parallel 1.26, tandem	0.0	0.0	0.0	1.0

was detailed in Ref. [17]. This simulation choose the H_2 -Air reaction mechanism proposed by Jachimowski [18] and including 9 species and 19 steps. An assumed sub-grid Probability Density Function(PDF) closure model was adopted the LES region. The modelling approach had been detailed in Ref. [19] and tested in previous works [20, 21]. The detailed NS equations could be referred to Ref. [15].

The air stream and fuel jet parameters for experimental and numerical studies are reported in Table 4.1. In the simulation, the CO_2 (mainly produced by the air heater) in the air flow was treated as nitrogen, since the adopted reaction mechanism neglects nitrogen oxidation. Based on Table 4.1, the calculation is normalized by the following reference parameters, $L_{ref} = d = 2$ mm (d denotes the injector exit diameter), $U_{ref} = u_{inf} = 1368.2$ m/s, $T_{ref} = T_{inf} = 753.8$ K, $\rho_{ref} = \rho_{inf} = 0.3832$ kg/m³, and $p_{ref} = \rho_{ref} U_{ref}^2 = 715.3$ kPa.

4.2.2 Formation of the Flame Kernel

The supersonic combustor is ignited at various ignition energies and positions. The CH^* and OH^* chemiluminescence are then captured to investigate the effects of ignition energy and position on formation of flame kernel. Section 4.2.1.1 gives the experimental setup.

4.2.2.1 Effect of Ignition Energy

The effect of ignition energy on ignition was studied with the ignition position at P2. A representative set of CH^* chemiluminescence images are shown in Fig. 4.15 with ignition energies $E_1 = 303.6 \pm 7.4$ mJ and $E_2 = 230.7 \pm 6.0$ mJ. The intensity of each pixel is normalized by the maximum intensity of all the pixels during the ignition process.

As shown in Fig. 4.15, for the ignition energy E_1 , the flame kernel at $40 \mu s$ is bright and located in the cavity middle. The flame kernel follows the flow direction in the recirculation zone, and by $120 \mu s$ it has moved to the leading edge, becoming smaller and less bright. After being anchored there, its strength grows slightly from 120 to $200 \mu s$. Then it begins propagating to the downstream at $200 \mu s$, and has filled the cavity by $560 \mu s$. After $80 \mu s$, the flame kernel spreads into the mainstream from

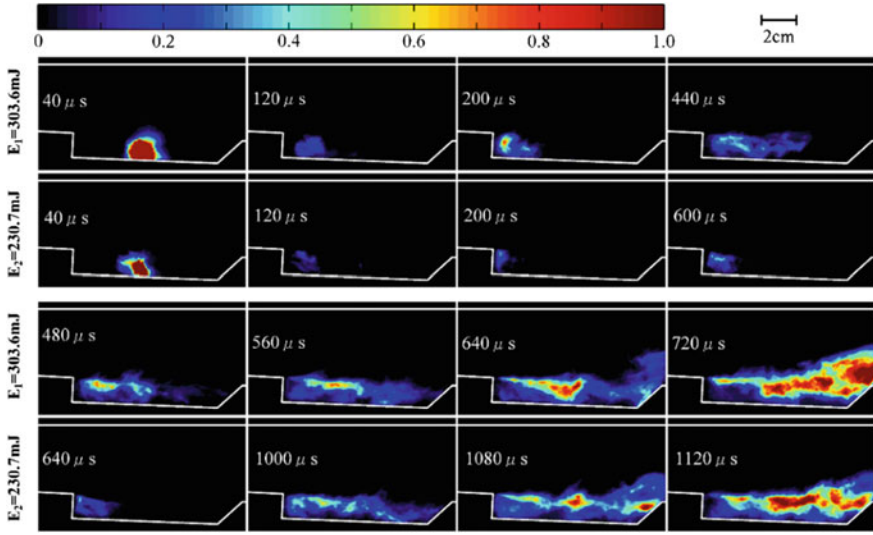


Fig. 4.15 CH* chemiluminescence images of ignition processes with ignition energies $E_1 = 303.6$ mJ and $E_2 = 230.7$ mJ [8]

the rear wall. At last, the combustor settles into the quasi-stable burning process by 720 μ s.

When the ignition energy is reduced to E_2 the initial flame kernel becomes smaller. It takes 1120 μ s for the flame kernel to fully fill the cavity and propagate to the mainstream, which is 400 μ s longer than the ignition process of E_1 . It is also noteworthy that the flame kernel is suppressed in the cavity during most time of the ignition process, because the high-speed flow and consequent high strain rate in the mainstream. In the quasi-stable burning process, besides, the flame intensity in the shear layer is much stronger than that elsewhere, because the air-ethylene mixture is rich in the shear layer.

4.2.2.2 Effect of Ignition Position

As represented by red spots in Fig. 4.10, three different ignition positions P1, P2 and P3 were used to investigate the effect of ignition position on formation of the flame kernel. The corresponding tests are then abbreviated as “Case P1”, “Case P2” and “Case P3”, respectively. All the tests shared an ignition energy of E_1 and a laser pulse frequency of 3 Hz.

A series of typical images are given in Fig. 4.16 to depict the flame spread processes with ignition positions at P1, P2 and P3. In Case P1 the initial flame kernel is adjacent to the leading edge, but it does not propagate downstream until 440 μ s after the laser pulse, which is 200 μ s later than the Case P2. Then it takes another 520 μ s for the flame kernel to fully fill the cavity. By 1040 μ s, a quasi-stable burning

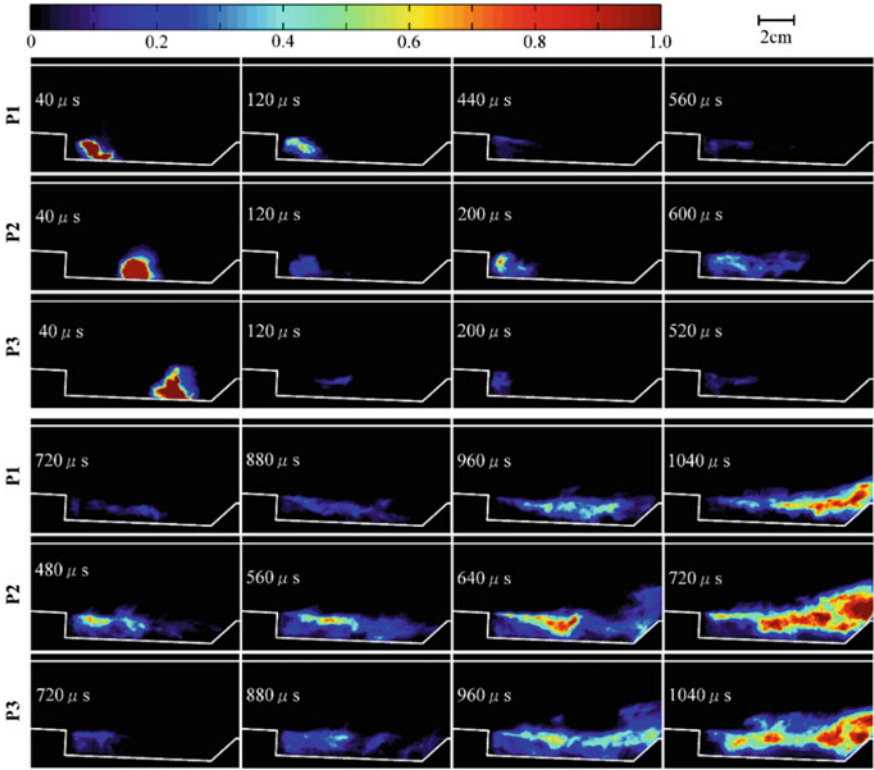


Fig. 4.16 CH* chemiluminescence images of ignition processes with ignition positions at P1, P2 and P3 [8]

process is achieved finally. If the ignition position is altered to P3, the initial flame kernel is the largest among these three cases. However, as the flame kernel spreads upstream, it shrinks in size and intensity strikingly, and arrived at the leading edge of the cavity by 200 μ s. During the subsequent 320 μ s, the flame kernel is anchored there without significant growth in size. Nevertheless, it begins propagating rapidly at 720 μ s. Additionally, the ignition position does not influence the flame structure in the quasi-stable burning process.

During the experiment the laser system operated at 3 Hz, which means that for two successive laser pulses the time interval was about 333 ms. Since this interval is much longer than the typical residence time (~ 1 ms) in scramjet combustors, the flowfields at different ignition moments were independent of each other, provided that the combustor was not ignited by the former laser pulses. Analyzing successful and unsuccessful ignition events provides more insights. Table 4.2 reports ignition probability for 4 cases and 32 tests (each case was repeated for 8 times), where η_i ($i = 1, 2,$ and 3) represents the probability that the combustor is successfully ignited by the i -th laser pulse. Assume η_s as the ignition probability for a single laser

Table 4.2 Ignition probability at different ignition energies and positions

Energy/position	η_1	η_2	η_3	η_s
303.6 ± 7.4 mJ/P2	0.875	0.125	0	0.87
230.7 ± 6.0 mJ/P2	0.375	0.500	0.125	0.42
303.6 ± 7.4 mJ/P1	0.500	0.375	0.125	0.50
303.6 ± 7.4 mJ/P3	0.625	0.375	0	0.62

pulse, then $\eta_s = \eta_1$, $(1 - \eta_s) \eta_s = \eta_2$, and $(1 - \eta_s)^2 \eta_s = \eta_3$. According to the values of η_1 , η_2 and η_3 given in the table, the ignition probability η_s for each case can be estimated via the least square method. As the ignition energy increases from 230.7 to 303.6 mJ, the estimated value of η_s is doubled. This indicates that with the current configuration, ignition in the cavity middle is superior among the three positions.

4.2.3 Flame Propagation in the Single-Cavity Supersonic Combustor

With the experiment setup described in Sect. 4.2.1.2, fifteen ignition cases are conducted as listed in Table 4.3 and each case is executed twice for ensuring repeatability. In the table, A, B and C represent three cavities with different rear wall heights. Each cavity pertains to five cases, in order to study the features of combustion flowfield and the effects of equivalence ratio.

Table 4.3 Experimental test conditions

Case	P_i (MPa)	ϕ	Ignition state
A1	0.96	0.14	✓
A2	1.30	0.20	✓
A3	2.05	0.31	✓
A4	2.69	0.40	✓
A5	3.56	0.53	✓
B1	0.94	0.14	✓
B2	1.28	0.19	✓
B3	1.94	0.29	✓
B4	2.66	0.39	✓
B5	3.46	0.53	✓
C1	1.03	0.15	×
C2	1.44	0.22	×
C3	2.03	0.30	✓
C4	2.74	0.41	✓
C5	3.58	0.54	✓

Previous numerical studies [10, 22] have revealed that the flowfield structure in the combustion with the rear-wall-expansion cavity would change greatly, and the cavity shear layer moves towards the bottom wall of the cavity, resulting in stronger turbulent dissipations and a smaller recirculation zone in the cavity. Thus, in the rear-wall-expansion cavity, the ignition environment would be exacerbated. As listed in Table 4.3, C1 and C2 failed to form a stable flame in the combustor, which indicates that for cavity C, it would be rather hard to achieve successful ignition when the equivalence ratio is lower than 0.3. This also demonstrates that the cavities A and B own a better ignition performance than C under low equivalence ratios.

4.2.3.1 Flame Propagation Routine

Figure 4.17 taken from the top view illustrates the flame propagation routine. The initial flame first propagates towards the leading edge of the cavity. After a short time, the initial flame grows stronger and propagates back towards the rear wall of the cavity. Finally, a steady flame is formed in the cavity. From $t = 0.6$ ms to $t = 0.7$ ms, it is noted that the initial flames near two side walls propagate faster than those in the middle part. This might be attributed to integrated effects of local equivalence ratios and turbulent flowfield in the cavity, which should be further investigated. The flame propagation routines of cases A3 and B3 present similar behaviors with that of case C3. However, the corresponding time spans of establishing a stable flame in the cavity are different, as shown in Fig. 4.18.

Figure 4.18 shows the difference of flame propagation among cases A3, B3 and C3 at $t = 0.8$ ms. All the three cases achieve successful ignitions at the equivalence ratio of 0.30. Nonetheless, both the flame propagation distance and the flame luminosity decrease from the top down, which indicates that lowering the rear wall height reduces

Fig. 4.17 Flame luminosity images (top view) of the flame propagation process of case C3 [14]

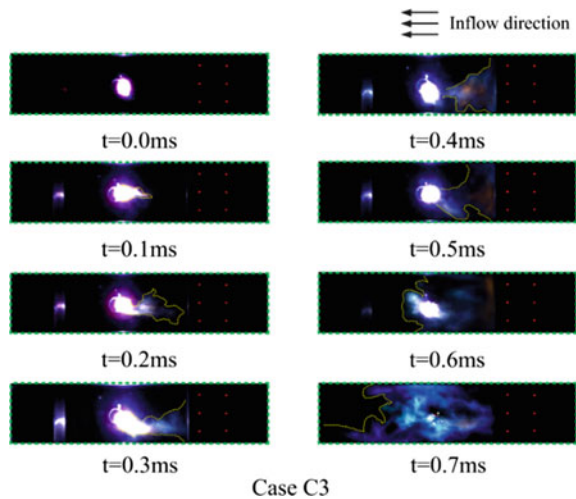
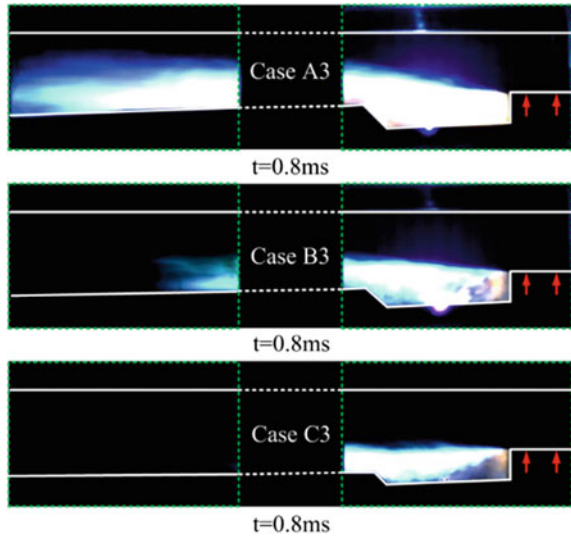


Fig. 4.18 Comparison of the flame propagation of cases A3, B3 and C3 at $t = 0.8$ ms [14]



the initial flame propagation. One possible reason is that lowering the rear wall height decreases the recirculation zone in the cavity and reduces the fuel entrained into the cavity. Therefore, the cavity with a large rear wall height is more favorable for ignition and flame propagation in a cavity-based supersonic combustor.

4.2.3.2 Reaction Zones Flashback Phenomenon

During the flame propagation process of cases A5, B5 and C5 with equivalence ratios close to 0.53, the reaction zone flashback phenomenon is observed. Figure 4.19 gives an example for the phenomenon captured in case C5. The brightest zones correspond to the most intense reaction zones. From $t = 1.2$ ms to $t = 1.5$ ms, the flame far downstream the cavity (the left side of the left window) grows thick, then the most intense reaction zones move upstream gradually. From $t = 2.7$ ms to $t = 3.3$ ms, the flame above the cavity becomes thick. As a result, a more evenly distributed flame is established in the combustor.

Widely existing in real scramjets, the reaction zones flashback phenomenon is a complex physical process closely related to the boundary layer separations. The phenomenon is probably induced by the upstream propagation of the combustion region with boundary-layer separation in the downstream weak combustion region [23]. It starts where the shockwave from the cowl lip crossed over the weak combustion region downstream the cavity at the initial phase of the ignition process. The transition is driven by the combustion-induced pressure rise. So the phenomenon usually occurs in the flame propagation process. Also, the combustion-induced pressure rise increases as the equivalence ratio becomes larger, which explains why the flashback phenomenon is clearly captured in cases A5, B5 and C5.

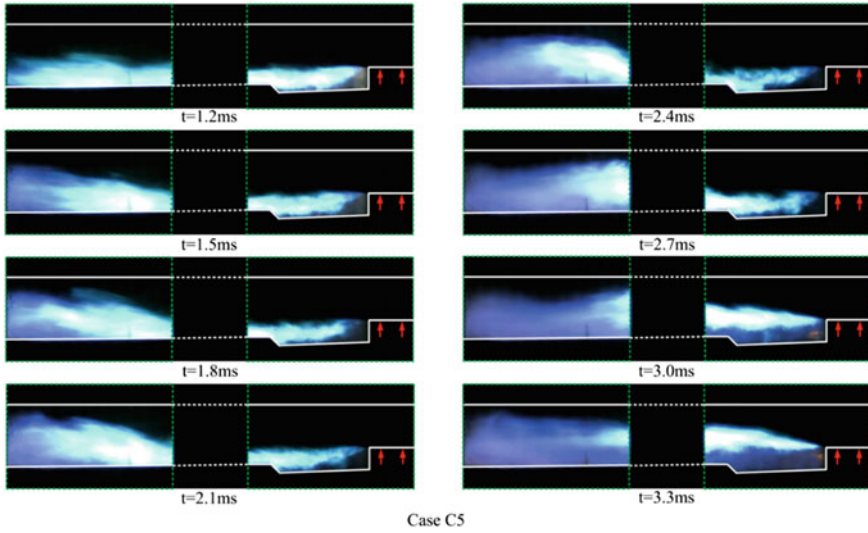


Fig. 4.19 Reaction zone flashback phenomenon during the flame propagation process of case C5 [14]

4.2.4 Flame Propagation in the Multi-cavity Supersonic Combustor

The ignition transients of hydrogen flame in a model scramjet combustor with parallel and tandem dual-cavity are separately simulated, along with the experimental observation on flame structure evolution. The numerical and experimental setups are given in Sect. 4.2.1.3.

4.2.4.1 Transient Process of Flame Stabilization in A parallel Dual-Cavity

Before reaching robust combustion, the cavity-stabilized jet flame would experience a transformation with the flame base moving around the cavities. For the parallel-dual cavity, a movement of flame observed experimentally is reproduced in simulation, as shown in Fig. 4.20.

In the transient process the reaction zone moves upstream, which is evident both from the flame luminosity images captured by a high-speed camera and the instantaneous temperature contours obtained in the simulation. Figure 4.20 shows three stages of flame structure during the stabilization process. Stage 1 relates the state just after the successful ignition, and stage 3 presents a periodic steady state. The time span for the three experimental images is 0.8 ms, and in the simulation changing

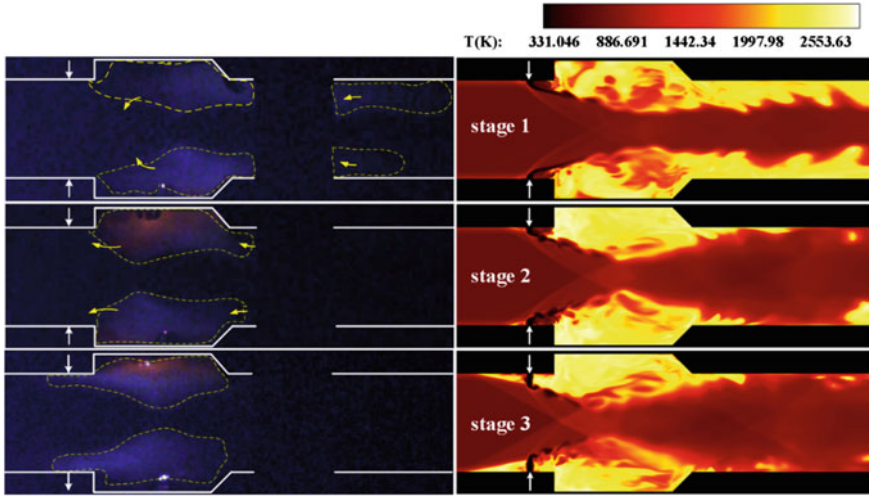


Fig. 4.20 Flame luminosity images captured by experiment (left) and instantaneous temperature contours in the central plane obtained by calculation (right) [15]

from stage 1 to stage 3 costs $487.5 L_{ref}/U_{ref} \approx 0.713$ ms. Therefore, the time scale for the transient process is of the order of magnitude of 1 s.

In regard of the transient process, the simulation coincides well with the experiment. The yellow arrowheads marked on the flame luminosity images indicate tendency of flame development. The flame stabilized by the cavities eventually extends its leading front to the region around the jet exit, and then a small combustion zone emerges and stabilizes in the recirculation zone upstream of the jet exit. The existence of this combustion zone makes the hydrogen jet penetrate deeper into the core flow. During the flame stabilization transient process, the reaction zone downstream of the cavity is reduced, and at the dual-cavity the flames gradually bulge to compress the core flow passage. It is observed that the flame structure shown in stage 3 is quasi-steady on the given condition for both the experiment and the simulation, and the temperature of the main combustion zones exceeds 2400 K. Hot products within cavities contributes heat and active radicals to fuel-jet mixing regions.

The spatiotemporal evolution of the non-dimensional heat release rate (HRR) flux in Fig. 4.21 explicitly reveals the movement of reaction zone upstream towards the leading edge of the cavity during the transient. HRR flux is denoted as

$$Flux_{HRR}(x) = \frac{1}{\Delta t} \int_0^{\Delta t} \oint_{A(x)} HRR(x, y, z, t) dydzdt$$

where Δt represents a time step and $A(x)$ the combustor sectional area at location x . HRR flux helps to quantify the evolution of combustion intensity and heat release in

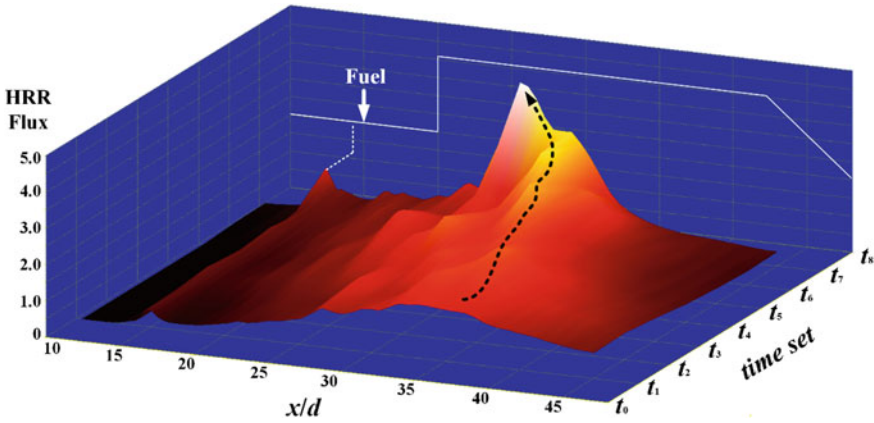


Fig. 4.21 Spatiotemporal distribution of non-dimensional heat release rate flux along the streamwise direction [15]

the combustor. In Fig. 4.21, the time set begins from t_0 to t_8 between which the whole transient process is captured, and t_8 is in stage 3 after which there exists no remarkable change in the distribution and magnitude of HRR flux, i.e., a quasi-steady combustion state has been reached. The HRR rate is computed with $\Delta t = 55.25 L_{ref} / U_{ref}$.

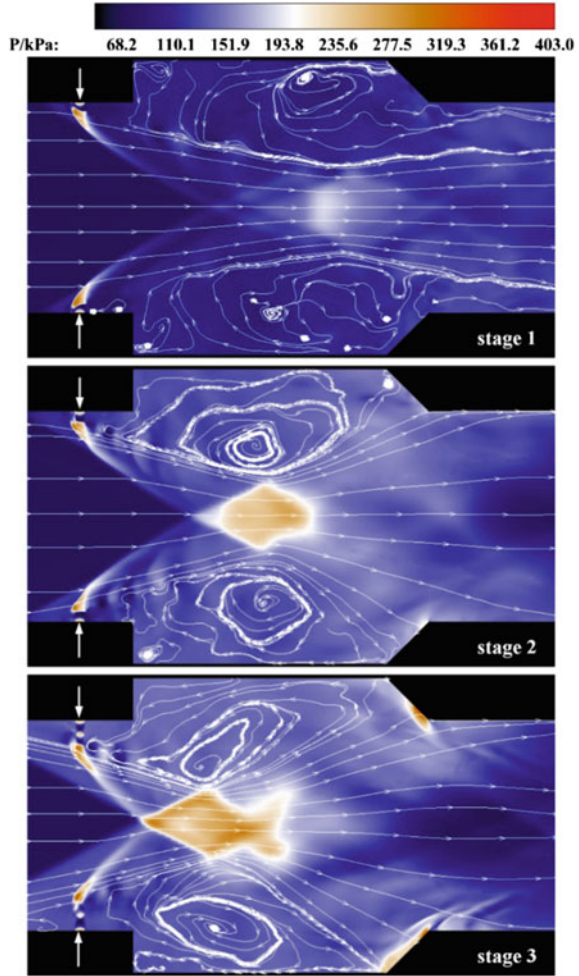
As plotted in Fig. 4.21, the magnitude of heat release rate increases rapidly during the upstream extending of the cavity-stabilized flame zone. HRR flux starts from 1.0 at t_0 , and then grows to about 4.0 at t_8 , arriving at a ‘heat peak’. The HRR flux history indicates the combustion becomes stronger during the transient process. After t_4 , the combustion mainly concentrates in the middle of the cavity, and then spreads over the front part. In addition, there is an increment of HRR flux around the Hydrogen jet exit, which is attributed to the ignition and flame stabilization upstream of the injection location.

Figure 4.22 illustrates the streamlines and pressure contours of different stages in the transient process. The first subfigure presents the central plane in stage 1 when the hydrogen jet is successfully ignited and the early-stage flame zone is being established. In stage 1, the pressure of the flowfield rises slightly, and the recirculation flow within the cavities is weak. At this moment, the flame anchors at the rear part of the cavity and squeezes the streamlines, thus the core flow fails to reattach the combustor floor downstream of the parallel cavities.

The second subfigure corresponds to stage 2 where the transient process is undergoing. The pressure rises around the cavities and a quite high-pressure region (240–280 kPa) appears in the core flow. The streamlines evidently show that a major vortex grows under/above the cavity shear layer and predominates the flow in the recirculation zones. The vortex cores near the high-pressure region compress the incoming flow. In contrast to stage 1, the core flow in this stage reattaches the rear walls.

The third subfigure presents an approximately steady state of the cavity-stabilized flame. A region with higher pressure can be observed in the core flow, indicating

Fig. 4.22 Calculated pressure contours together with streamlines in the central plane of three stages [15]



stronger combustion overall. The high-pressure region, compared with that at stage 2, moves toward the combustor inlet. This movement coincides with the combustion region change shown in Fig. 4.20. Similarly, the predominating vortices in the recirculation zones experience a transformation and then lift the cavity shear layers. It is noteworthy that the flow and combustion in parallel cavities perform asymmetric characteristics provided with the same geometry, mesh and simulation conditions for the two cavities.

The profiles of streamwise velocity and temperature related to the transient process are shown in Fig. 4.23. The figure includes the data at axial locations $x/d = 20$ (the leading edge of the cavity) and $x/d = 44$ (the bottom edge of the rear wall), in order to emphasize the variations of core flow from stage 1 (blue) to stage 3 (red). From Fig. 4.23a and c, the faster and cooler inlet gas is compressed from $y/d = 2 \sim 18$ at

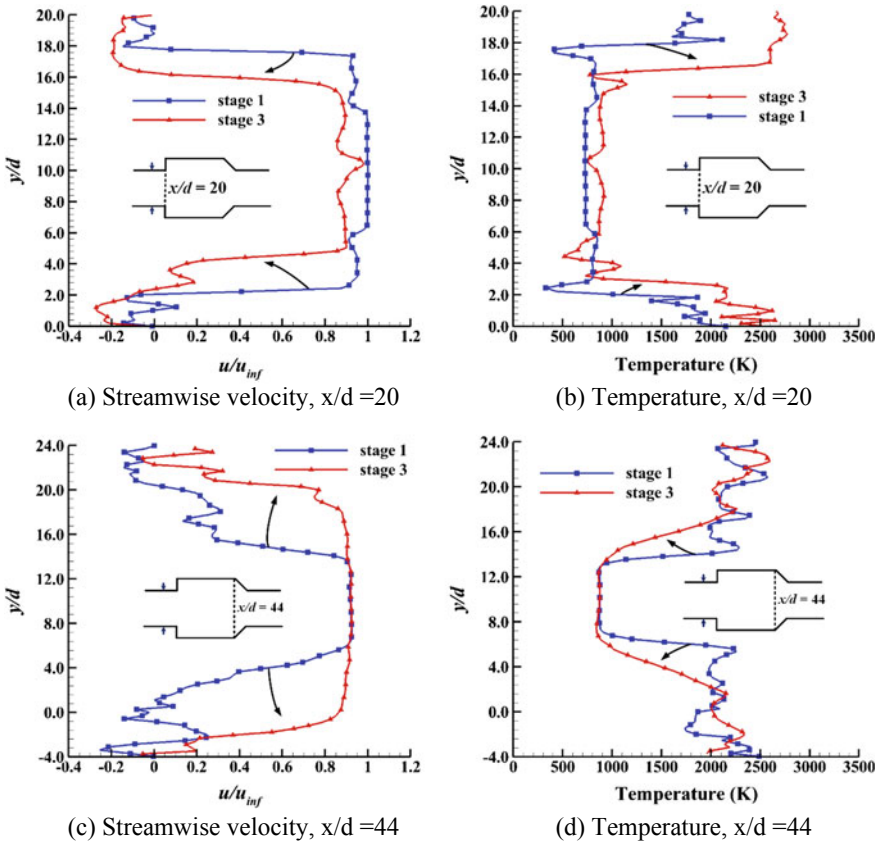


Fig. 4.23 Calculated profiles of streamwise velocity and temperature at two streamwise locations in the centralplane [15]

stage 1 to $y/d = 4 \sim 16$ at stage 3, and at the same time the core flow expands near the rear wall of the cavity. As plotted in Fig. 4.23c, the streamwise velocity at stage 1 regains 90% of u_{inf} in $y/d = 5-15$, but at stage 2 the range varies to $y/d = 0-20$. Figure 4.23d further denotes that the hot combustion region (around 2500 K) gets closer to the cavity floor. The whole behaviors are consistent with the observation in Fig. 4.20.

Figure 4.24 shows composition concentrations and non-dimensional HRR in the spanwise plane at the middle of the parallel cavities. The region with high HRR mainly concentrates in the jet shear layer. Further, both the region size and the HRR rise as the fuel jet penetrates deeper during the transient process. As plotted in the bottom left subfigure, hydrogen concentration gets weaker and the hydrogen spreads more widely around the cavities, denoting much fuel is consumed upstream of this spanwise plane and more fuel is entrained into the cavities. According to the bottom right subfigure, it is noted that the OH radicals chiefly appear in the recirculation

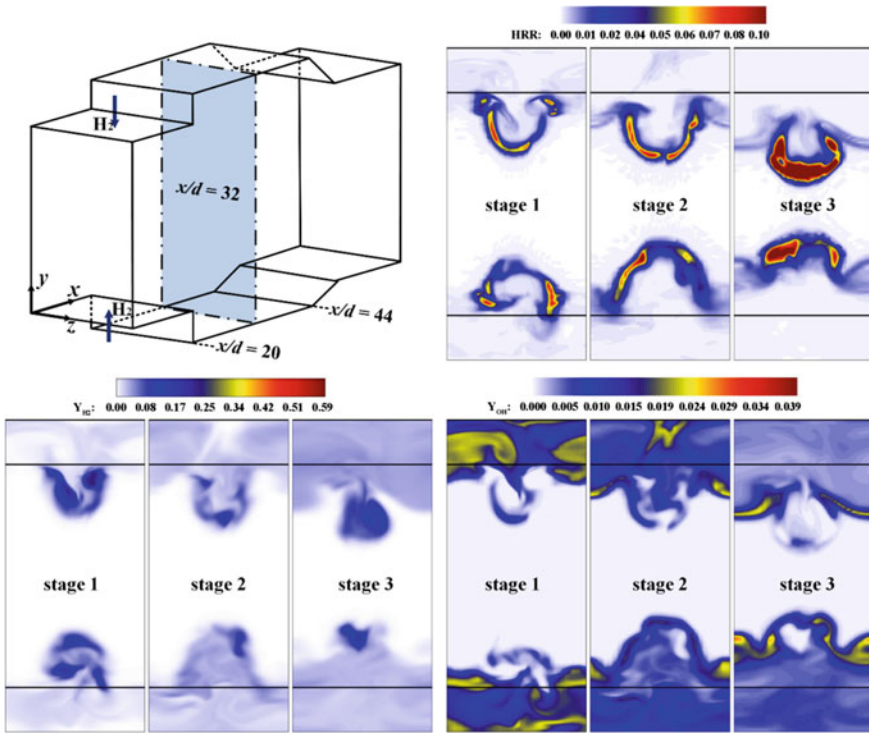


Fig. 4.24 Heat release distribution and OH, H₂ mass fractions in plane $x/d = 32$ [15]

zones at stage 1, then the concentration decays quickly within the two cavities during stage 2, and eventually in the shear layers are found the OH radicals at stage 3. This shift reflects the transient behaviors within recirculation zones.

Based on the above discussion from Figs. 4.20, 4.21, 4.22, 4.23, 4.24, it is illustrated in Fig. 4.25 that the mechanism of the transient process from ignition to flame stabilization, with respect to the dual-cavity. The flame evolution during the transient process may be attributed to positive feedbacks among the three sub-processes, involving (1) the strong heat release and hot products generating from jets and shear layers, (2) the recirculation zones where the major vortices stir whilst transfer active radicals, and (3) highly-pressurized combustion zones extending and compressing the incoming core flow. During the whole transient process, reaction keeps robust in the shear layers and the high-temperature reactants are continuously transferred into the recirculation zones. The initial flame caused by successful ignition is anchored near the rear parts of the parallel cavities, which helps to accumulate active radicals. Meanwhile, the major vortices are being built, and then accelerate the transport of energy and reactive chemicals into the fresh premixing fuel/air gas around the leading edges. Also, high pressure in the recirculation zones further enhances the combustion in them. As time pushes forward, therefore, larger robust combustion zones

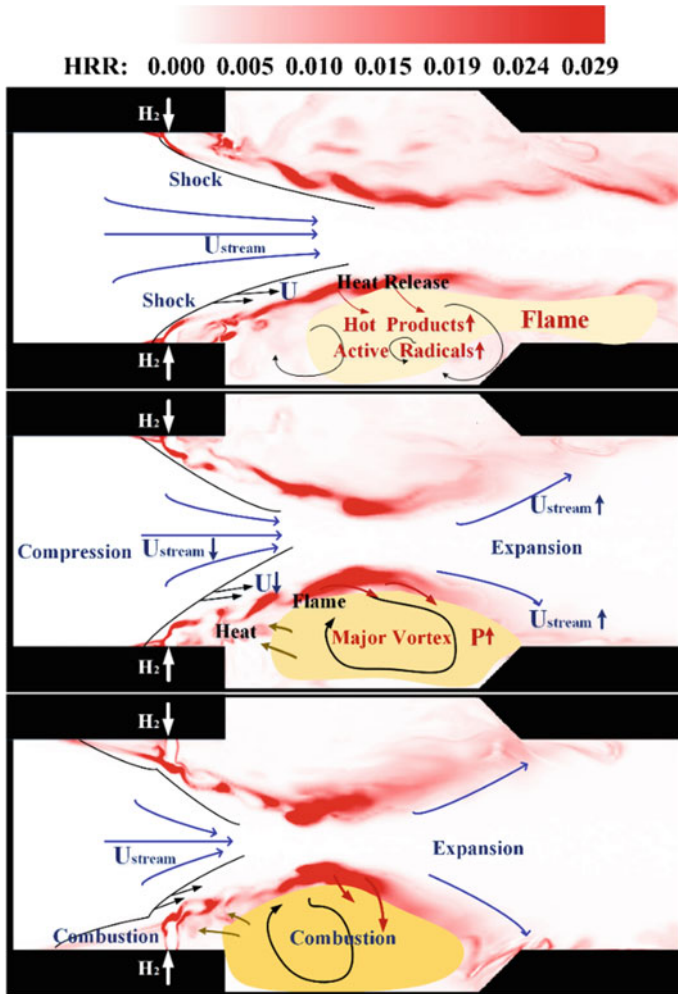


Fig. 4.25 Schematic of flame stabilization transient process in parallel dual-cavity [15]

are established in the parallel cavities. With the interaction of flame and shockwave developing from the two cavities, strong reaction regions quickly move upstream along the shear layers, consuming more fuel within a short distance downstream of the jet exits. On the other hand, the expanding recirculation zones also compress and slow down the core flow, in turn enhancing the premixed or partially-premixed combustion in the jet wakes. The process witnesses a quick lift of jet penetration, and a significant upstream movement of strong combustion zones in the dual-cavity. After that, dual-cavity-stabilized flame climbs over the leading edges, finally getting stabilized in the separation zones of the two jet exits.

4.2.4.2 Transient Process of Flame Stabilization in A tandem Dual-Cavity

For the tandem dual-cavity, dynamic characteristics of the flame transients are also well captured using the simulation approach, as shown Fig. 4.26. The three images on the left and right have a time interval of 0.6 and 0.665 ms, respectively. Both the experiment and the simulation reveal that the flame front displaces from the downstream cavity to the upstream cavity, during which the ‘stabilization base’ for combustion seems to propagate through the region between the two cavities. According to the experimental images, during the transient process flame is initially stabilized along the downstream cavity shear layer, and is then pushed forward. At the same time, a flame packet anchored by the upstream cavity emerges, as plotted in the left middle image. After that, in the combustor presents a robust flame throughout the two cavities.

Nonetheless, there is a minor distinction between the experiment and the simulation. As shown in Fig. 4.26, flame in the experiment is totally invisible in the upstream cavity at stage 1, but in the simulation the flame is evident that there is a small high-temperature region near the rear wall. This distinction may be attributed to a combination of several factors, including the limited resolution in experiment, the reduced-chemical mechanism, the mesh quality in simulation, etc. Although the simulation fails to accurately reproduce the transient process, it roughly captures the related phenomena. The major reaction zones in the tandem dual-cavity show a relatively lower temperature than in the parallel dual-cavity, via the comparison of instantaneous temperature between Figs. 4.18 and 4.26. This may demonstrate that the parallel dual-cavity configuration together with the opposite fuel injections could strengthen combustion around cavities.

Existence of OH radicals in the hydrogen/air mixture can be viewed as an evidence for presence of combustion. Figure 4.27 shows the OH mass fraction distribution in the plane $y/L_{ref} = -1$ within the upstream cavity (left) and the downstream cavity

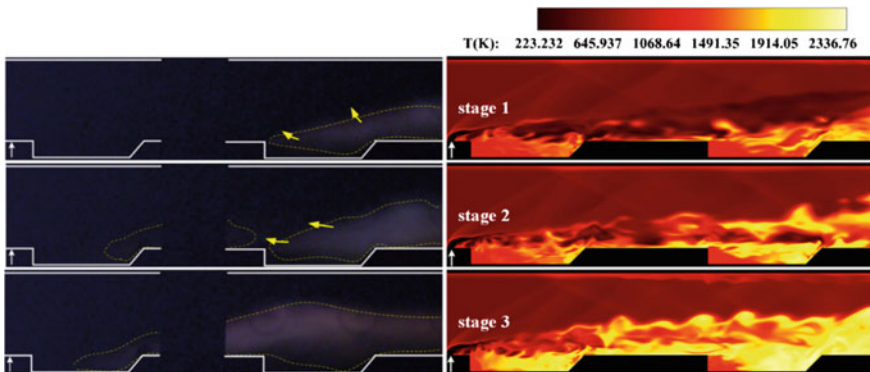


Fig. 4.26 Flame luminosity images captured by experiment (left) and instantaneous temperature contours in the central plane obtained by calculation (right) [15]

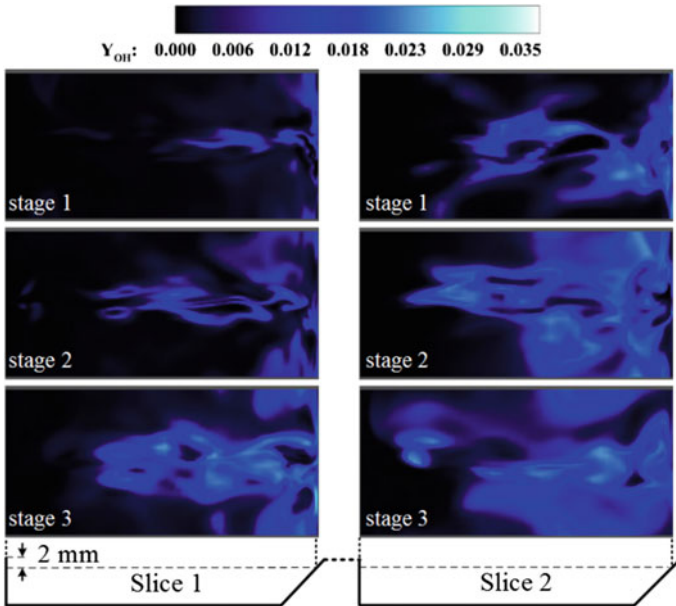


Fig. 4.27 The development of OH mass concentration in two vertical slices with the tandem cavity [15]

(right), respectively. Both the planes have a 2-mm distance below the cavity lips, as labelled in the figure. The OH mass fraction variation clearly depicts how the combustion is organized within the recirculation zones of the two cavities during the transient process. Specifically, there is a plenty of OH radicals in the downstream plane, indicating the initial flame observed both in the experiment and the simulation. From stages 2 to 3 the transient process occurs with the combustion region expanding spanwisely and toward the front parts of the two cavities.

In order to display the translational flame motion in the tandem dual-cavity, Fig. 4.28 shows the 2000 K temperature iso-surfaces where the colors represent the HRR. Variation of the high-temperature iso-surface between different stages delineates the development of main reaction regions from the downstream cavity to the upstream cavity. During the transient process, high-temperature regions caused by jet flame quickly roll up, enlarging themselves streamwisely and spanwisely. It takes less than 1 ms for the flame to conquer the upstream cavity. At stage 3, a strong combustion is stabilized by the two tandem cavities, and the high temperature regions further expand along the streamwise direction from the upstream cavity to the computational combustor exit. The HRR magnitude shown on the iso-surfaces reveals evolution of chief heat release regions. At stage 1, the heat release mainly concentrates near the downstream cavity and comes from initial flame packets. Then the strong heat release regions quickly move upstream, as plotted in the middle iso-surface. At stage 3, the core heat source is situated downstream of the fuel jet, and

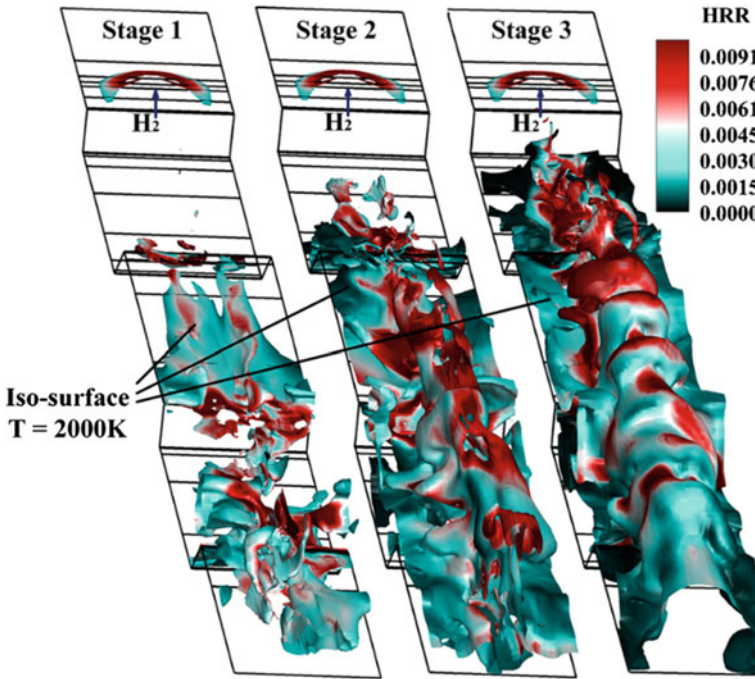


Fig. 4.28 Temporal growth of 2000 K iso-surface where the colour represents HRR [15]

stabilized by the upstream cavity. Figure 4.28 agrees well with flame luminosity images obtained by high-speed cameras.

Figure 4.29 shows HRR flux along the streamwise direction throughout the computational combustor. For stage 1, HRR flux has large values in $100 < x/d < 120$, near the rear wall of the downstream cavity. At stage 2, HRR flux then concentrates in $50 < x/d < 80$, between the two cavities. When stage 3 is reached, HRR flux peaks around $x/d = 65$. The results reveal where the strongest combustion exists and how it is established in the transient process lasting about 1 ms.

A plausible mechanism is illustrated in Fig. 4.30 to explain phenomena observed in the transient process. In the downstream cavity, initial flame generates a heated region with increasing pressure around it. This hot and active region combines with small flame packets anchored at the rear wall of the upstream cavity to produce larger flow separation between the two cavities. The separation zone has more appropriate conditions for combustion, the fuel ignition delay in the zone being reduced. As more hydrogen is consumed in the downstream cavity, the flame begins to propagate upstream, then merges with the flame in the upstream cavity, finally forming a robust flame. Though flame exists in the upstream cavity, the entire flame development is dominated by the combustion in the downstream cavity. In the separation zone the appropriate conditions, possibly ascribed to heat and radical transfer from the two cavities and the pressure rise, accounts for the fast flame motion.

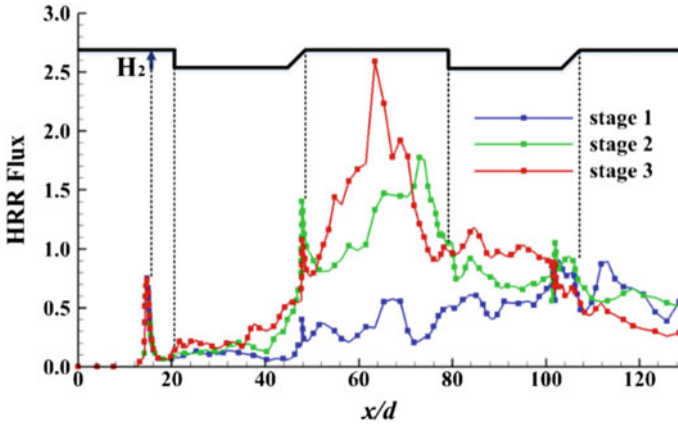


Fig. 4.29 Streamwise HRR flux distribution of three stages in the transient process of the tandem dual-cavity [15]

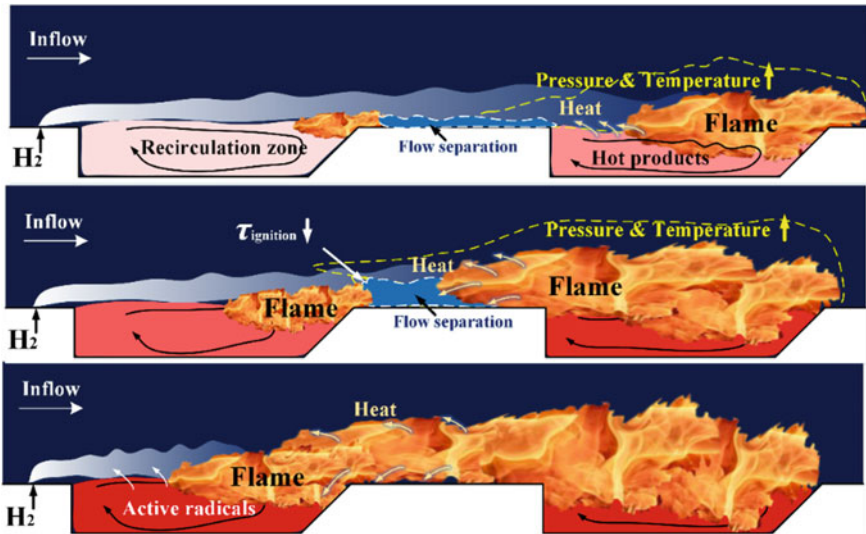


Fig. 4.30 Schematic of mechanism of the flame transients in the tandem dual-cavity [15]

4.3 Ignition Mechanism Analysis

The main purpose of studying the ignition process in a supersonic flow is to comprehensively reveal the ignition mechanism explaining diverse ignition behaviors. In this section, the ignition mechanism is clarified by introducing ignition stages as well as ignition modes.

4.3.1 Experimental and Numerical Setups

The supersonic inflow conditions and experimental facility have been introduced in Sect. 4.2.1.1. Details of the test facility can be found in Refs. [20, 24]. Information about the injectors are referred to Ref. [25]. The experiments conducted in Sects. 4.3.2 and 4.3.3 are based on LIP ignition and share the same cavity geometry, but with different imaging systems.

4.3.1.1 Experimental Setups

A photo for the LIP ignition experiments in Sect. 4.3.2 is presented in Fig. 4.31. The combustor was equipped with a typical rear-wall-expansion cavity. As shown in Fig. 4.32a, the leading edge depth, rear wall depth, floor length and aft ramp angle of the cavity were 20 mm, 10 mm, 90 mm and 45°, respectively. The upstream wall of the cavity was in parallel with the downstream wall. Two porthole injectors with a diameter of 2 mm were situated 10-mm upstream of the cavity, dividing the spanwise plane equally. Ethylene fuel was injected vertically to the inflow at the room temperature. The global equivalence ratio was respectively set to 0.16, 0.30 and 0.48, corresponding to the fueling stagnation pressures of 0.8 MPa, 1.5 MPa and 2.4 MPa. The fuel injection lasted for 1 s. Two quartz windows with a thickness of 20 mm were embedded into the side walls of the combustor.

Figure 4.32a plots the LIP ignition positions in the central plane. Ignition positions $a-1$, $b-1$, $c-1$, $d-1$, $e-1$, and $f-1$ have different horizontal distances to the leading edge,

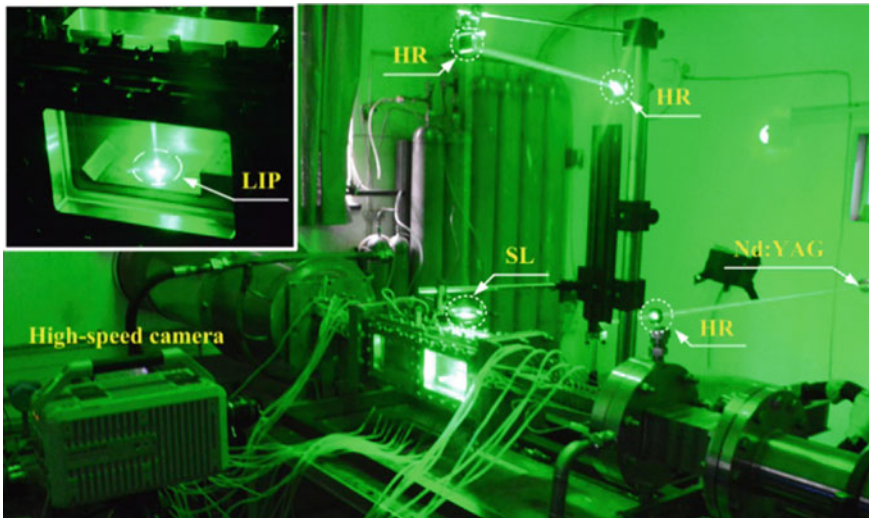


Fig. 4.31 Photo of the LIP ignition experiment facility [26]. The upper-left photo shows the combustor with incident laser

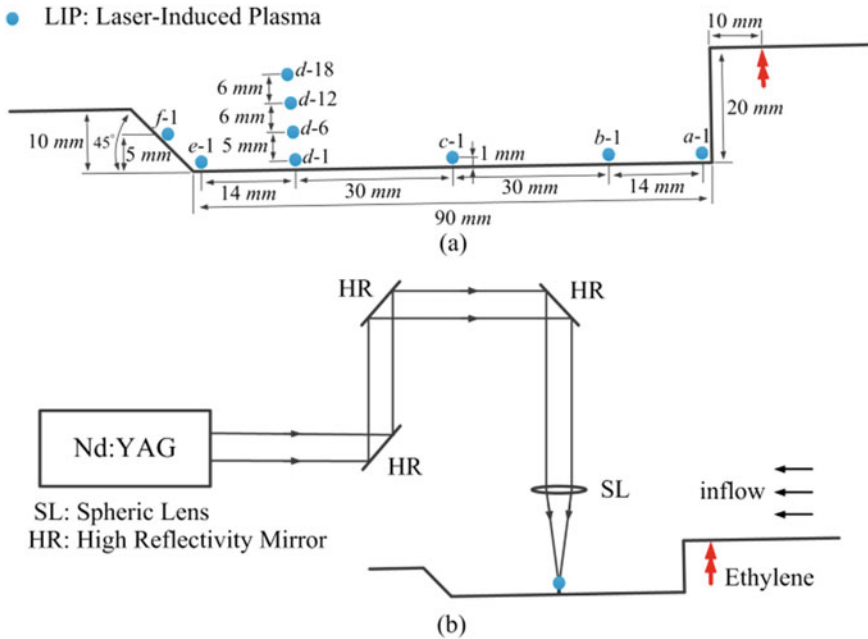


Fig. 4.32 Schematic of **a** the LIP ignition positions and the cavity, and **b** optical arrangement of LIP ignition experiments [26]

but their vertical distances to the cavity floor are all 1 mm. Ignition positions *d-1*, *d-6*, *d-12* and *d-18* are aligned vertically with different heights. Two fuel injectors were placed symmetrically about the central plane, and the distance of each injector to the central plane equals 8.4 mm.

The optical arrangement for the LIP ignition is shown in Fig. 4.32b. A frequency doubling Nd:YAG laser output 532-nm laser pluses with a pulse duration of 10 ns for ignition. After guided by several high-reflectivity (HR) mirrors, the laser beams were focused by a spherical lens (SL, $f = 130$ mm) in the central plane and above the cavity. Since the major laser energy is absorbed by the mixture, the energy reflected by the bottom wall is negligible. The laser pulse energy was kept at 300 mJ, and the absorbed energy approximately equalled 250 mJ.

The ignition and flame propagation processes were visualized by a high-speed camera (FASTCAM SA-X2) with a $f/1.4$ Nikkor lens. The camera worked at 50 kHz with a resolution of 768×328 pixels and an exposure time of $18 \mu\text{s}$. A 10-nm bandpass filter centered at 431 nm was mounted before the camera to collect CH^* chemiluminescence. The laser system and the camera were synchronized via a digital delay generator (DG645).

The LIP ignition process was also characterized by a schlieren system composed of a high-speed camera (FASTCAM SA-X2) equipped with a Nikkor lens ($f = 200$ mm, $f/4$). Both the two high-speed cameras share the same settings. Additionally, the wall

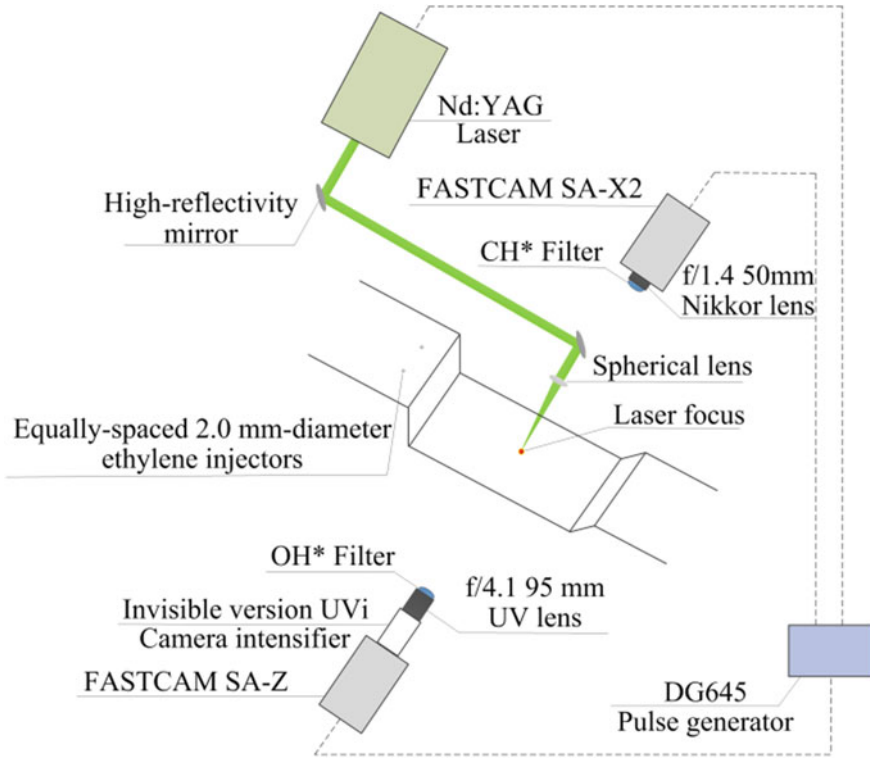


Fig. 4.33 Schematic of the experimental setup [28]

pressure along the combustor floor was measured through 32 static pressure taps with a sampling frequency of 100 Hz. The pressure transducers had an uncertainty of $\pm 0.5\%$ FS (full scale) [27].

The experimental setups in Sect. 4.3.3 are illustrated in Fig. 4.33. Configurations of the laser system and the optical paths were similar to that in Sect. 4.3.2. The laser beams were focused 1 mm above the cavity floor. The laser pulse energy was set as 200 mJ/pulse or 300 mJ/pulse. The efficiency of laser energy absorption was approximately 80%. It is noteworthy that two high-speed cameras simultaneously and respectively captured CH* and OH* chemiluminescence from two opposite sides of the combustor. The first camera (FASTCAM SA-X2) was equipped with a Nikkor lens ($f = 50$ mm, $f/1.4$) and a bandpass filter (centered at 431 nm, with a 10-nm FWHM). Another camera (FASTCAM SA-Z) utilized a camera intensifier (Invisible version UVI), a UV lens ($f = 95$ mm, $f/4.1$) and a bandpass filter (centered at 311 nm, with a 10-nm FWHM) to capture the OH* chemiluminescence. Both the cameras had an image frequency of 10 kHz, a resolution of 1024×512 pixels and an exposure time of $98 \mu\text{s}$. A digital delay generator (DG645) synchronized the laser system with the two cameras to make the LIP ignition process be recorded precisely.

Schlieren imaging were widely employed to reveal the flow structures in supersonic flowfield [29, 30]. In Sect. 4.3.3, the flow structures during LIP ignition process were then visualized via schlieren imaging. The schlieren system consisted of a high-speed camera (FASTCAM SA-X2) with a Nikkor lens ($f = 200$ mm, $f/4$). The camera operated at a frame rate of 50 kHz, with a resolution of 768×304 pixels and an exposure time of 18 μ s.

4.3.1.2 Numerical Setups

In Sect. 4.3.2, the fuel/air mixing and the flow structures before LIP ignition were studied through the large eddy simulation (LES). The LES equations were solved by Scramjet Foam [10], a solver modified from Open FOAM [31]. The solver utilized the Euler backward scheme for temporal integration and a second-order Gauss filtered linear scheme to discretize the diffusion terms. In the solver, the convective terms were discretized using the Kurganov and Tadmor scheme with the Van Leer Limiter. Thus, second order accuracy in both time and space could be achieved. The normalized grid resolution in the cavity where the mixing took place was $\Delta x^+ \approx 1-60$, $\Delta y^+ \approx 1-40$ and $\Delta z^+ \approx 20-60$.

A 3D structured grid with a size of 11,690,775 was used. The cavity region where mixing took place had normalized grid resolutions of $\Delta x^+ \approx 1 \sim 60$, $\Delta y^+ \approx 1 \sim 40$ and $\Delta z^+ \approx 20 \sim 60$. The inflow condition was in accordance with that in the experiments. The ethylene injection had a stagnation pressure of 1.5 MPa, corresponding to a global equivalence ratio of 0.3. References [10, 11, 22, 32] detailed the numerical methods.

4.3.2 *Four-Stages Dominated Ignition Process*

Spark ignition and flame motions in the scramjet combustor with a rear-wall-expansion geometry has been studied both experimentally and numerically [12, 13, 32, 33]. In this section, experiments were performed to investigate LIP ignition processes in a rear-wall-expansion cavity model scramjet combustor with an inflow of $Ma = 2.92$. The LIP ignition and related combustion dynamics were investigated using CH* chemiluminescence imaging at 50 kHz. The results indicate that the ignition and flame stabilization are sensitive to the LIP location. To further understand the LIP ignition process in the combustor, large eddy simulations were conducted to characterize the mixing field and the flow dynamics. On basis of the experiments and the simulation, the LIP-assisted ignition in a cavity-based scramjet combustor is explained fundamentally.

4.3.2.1 Ignition Process in the Cavity

First, the initial flame propagation process within the rear-wall-expansion cavity is examined. The LIP ignition experiment was executed two times to observe the repeatability in each ignition position. The ignition results are presented in Fig. 4.34, where the red dots indicate the locations at which successful ignition and sustained combustion are achieved, and the black dots denote ignition failure. In *f*-1 and *d*-18, the ignition failed at all global equivalence ratios (Φ), but in ignition positions *a*-1 and *b*-1 the ignition was unsuccessful only at $\Phi = 0.16$. Successful ignition was achieved at all equivalence ratios for *c*-1, *d*-1, *e*-1, *d*-6 and *d*-12.

Processes of ignition and initial flame propagation were visualized through the high-speed imaging of CH^* chemiluminescence and schlieren. CH^* has been shown as a good marker of local reaction zones [34]. The high-speed imaging of CH^* chemiluminescence shows the flame-front and heat-release regions on a time-resolved basis without spatial blurring, and the schlieren images indicate the density gradient.

Figure 4.35 gives the experimental observation with LIP ignition at *e*-1. The LIP ignition (with a laser pulse of 10 ns) event happens at $t = 0 \mu\text{s}$. It is seen that 20 μs after the LIP ignition, a rather large region of high CH^* chemiluminescence appears around the ignition position where the schlieren image shows a white zone with saturated pixel intensities. The LIP energy focused on the ignition position results in an ultra-high temperature region (e.g. with a temperature possibly as high as 4000–16,000 K [35]) where the gas molecules undergo complex processes such as dissociation, atomization, ionization and excitation. Due to the large temperature and concentration gradients across the boundary of LIP ignition region, the high

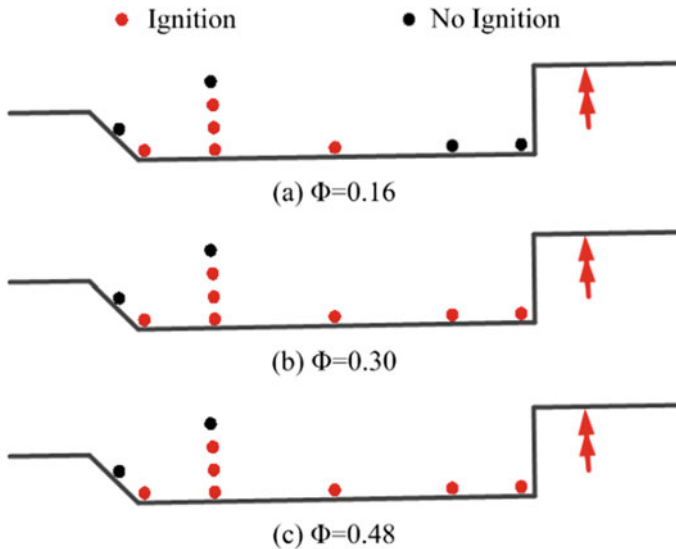


Fig. 4.34 Schematic of the LIP ignition results [26]

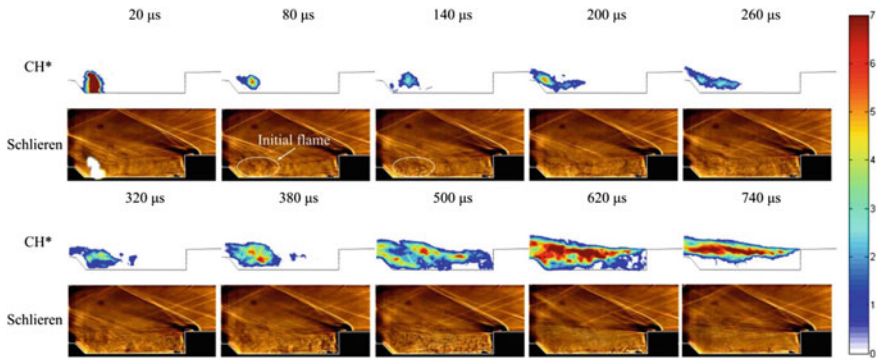


Fig. 4.35 Images of CH* chemiluminescence and schlieren after LIP ignition at $e-1$ with $\Phi = 0.30$ [26]

temperature gas around the region diffuses into the ambient colder fuel/air mixture. This diffusion cools the region and reduces the intensity of CH* chemiluminescence, as shown at $t = 80 \mu\text{s}$. The region enclosed by the white ellipse shows finer structures with variation of density gradients than that the ambient, which denotes in this region significant heat and mass transfer. Moreover, this region is much larger than the region where exists observable CH* chemiluminescence.

It is expected that the temperature in the surrounding gas could initiate the chemical reactions, which is confirmed in the schlieren and CH* chemiluminescence images at $140 \mu\text{s}$ that some signals are detected outside the main signal region. As shown in the subfigures from 140 to $500 \mu\text{s}$, the region of CH* radicals develops inside the cavity toward the injector. At $740 \mu\text{s}$ after LIP ignition a flame is then well stabilized. This observation is consistent with the results in Ref. [8], where the initial ethylene flame propagated first towards the leading edge and then spread downstream, regardless of the LIP ignition position in the cavity.

As depicted in Fig. 4.35, during 500 and $620 \mu\text{s}$ the CH* signal is found in nearly the entire cavity, which means the fuel in the cavity is consumed quickly. Thereafter, the main combustion occurs in the shear layer. As a result, the fuel entrained into the cavity becomes much less. The cavity then acts as a reservoir filled with hot products and radicals (e.g. OH) that stabilizes the flame in the shear layer [22]. This is confirmed by the signal distribution at $740 \mu\text{s}$.

Figure 4.36 plots the integration of signals over each CH* chemiluminescence image during the ignition, with respect to different fuelling rates. The integrated signals are normalized by the mean value obtained at the stable flame stage. Very high integrated signal appears before $50 \mu\text{s}$, corresponding the LIP ignition event. When $\Phi = 0.30$, the integrated signal increases from $50 \mu\text{s}$ and then peaks at $600 \mu\text{s}$. In this period, as shown in Fig. 4.35, the flame propagates into and fills the entire cavity. Thereafter, the integrated signal initially decreases and then oscillates around the mean value after $740 \mu\text{s}$, since a flame has been stabilized in the shear layer. With different fuelling rates, the integrated signal presents similar trends. However,

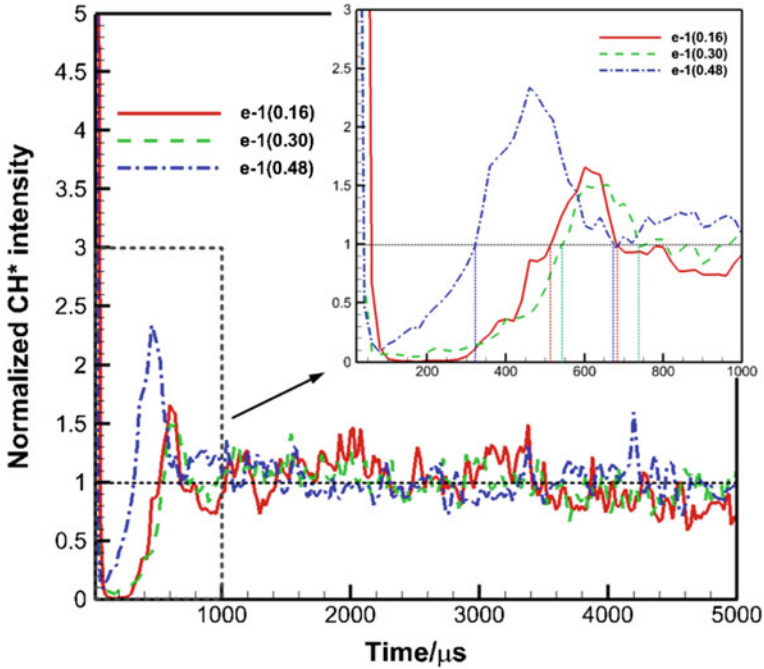


Fig. 4.36 Integrated CH* chemiluminescence intensity against time after LIP ignition at $e-1$ with $\Phi = 0.16, 0.30$ and 0.48 [26]

the flame development with a higher fuelling rate ($\Phi = 0.48$) takes a shorter time (from 50 to 420 μs), possibly because the fuel-richer mixture in the cavity is more in favor of ignition process. Another perceptible difference in the ignition process for the three fuelling rates is shown in Fig. 4.37. With a lower fuelling rate ($\Phi = 0.16$), there is no CH* chemiluminescence observed in the bottom right of the cavity. This phenomenon is mainly due to the low local equivalence ratios, which will be discussed in next section.

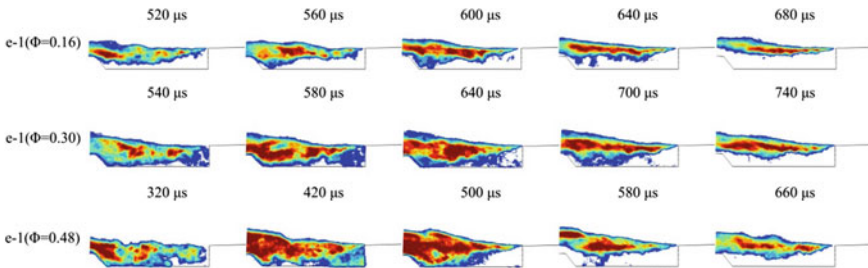


Fig. 4.37 CH* chemiluminescence images after LIP ignition at $e-1$ with $\Phi = 0.16, 0.30$ and 0.48 [26]

4.3.2.2 Mechanism of Cavity Ignition

Exploring the mixing field and the flow structure in the cavity helps to understand key factors leading to ignition of mixture in the cavity. Figure 4.38 shows contours of the velocity, the Mach number and the local equivalence ratio in the cavity and the shear layer prior to the LIP ignition event. The contours come from LES of the case $\Phi = 0.30$. Detailed LES results will be given in the next section, where the numerical accuracy and comparison with experiments are presented, as well as the three-dimensional mixing field and enstrophy field.

According to Fig. 4.38, the flow decelerates rapidly across the shear layer. The flow velocity decreases from Mach numbers greater than 1 in the free stream outside the cavity to rather low Mach numbers inside the cavity. Meanwhile the flow inside the cavity forms a large recirculation zone. Partial fuel/air mixture in the shear layer entrances into the cavity along the rear wall, and then flows towards the leading edge, and finally moves upward to the free stream. The recirculating flow inside the cavity convects the plasma/gas mixture from the LIP ignition position $e-1$ (illustrated in Fig. 4.32) to the leading edge. The hot mixture acts as a heat and radical source that eventually ignites the flammable mixture inside the cavity. Once the mixture inside the cavity is sufficiently burned, the cavity functions as a flame holder that continuously ignites the fuel/air mixture in the shear layer.

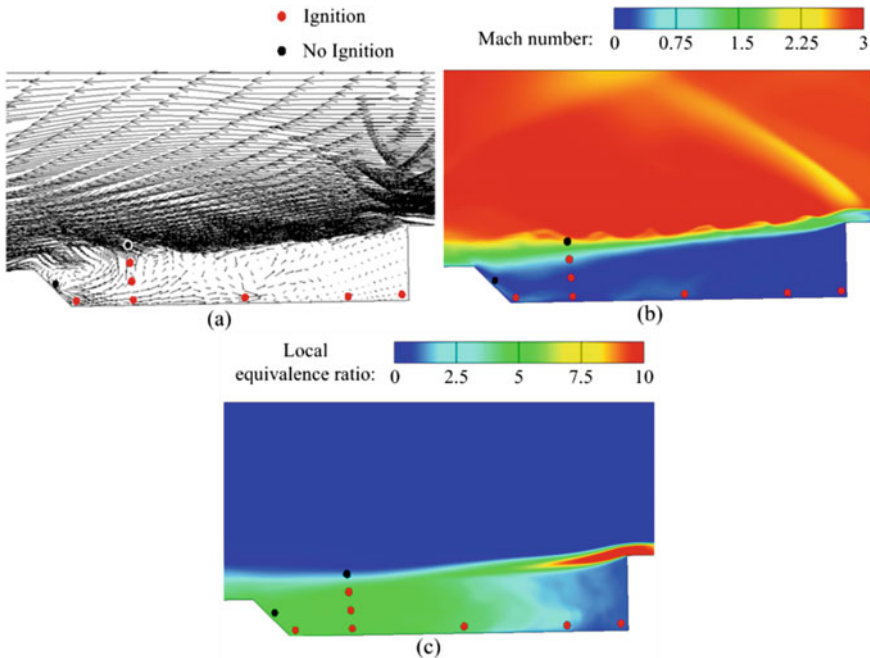


Fig. 4.38 Distributions of **a** velocity vector, **b** Mach number, and **c** local equivalence ratio. The results are from LES with $\Phi = 0.30$ [26]

Since the LIP positions $d-18$ and $f-1$ are located outside the recirculation zone, the generated plasma/gas mixture is convected directly downstream and then quenched due to the locally high Mach number. This explains the ignition failures for LIP ignition at $d-18$ and $f-1$. The LIP positions $d-6$ and $d-12$ are in the recirculation zone and thereby a stable flame is formed. Although the LIP positions $a-1$ and $b-1$ are inside the recirculation zone, the plasma/gas mixture formed in the two positions has a much shorter resident time in the cavity than the other cases, since the positions are close to the leading edge. Such short resident time limits the heat released by interaction of the plasma, the fuel and the air in the cavity, especially when the local equivalence ratio is low. This might explain why the LIP ignition at $a-1$ and $b-1$ with $\Phi = 0.16$ fails, since the small amount of heat release is unable to ignite the shear layer.

To confirm the above discussion, the CH^* chemiluminescence images with LIP ignition at $a-1$ and $\Phi = 0.30$ are shown in Fig. 4.39. The initial signal from the LIP around $a-1$ lasts for $260 \mu\text{s}$. From 320 to $580 \mu\text{s}$, the CH^* chemiluminescence quenches when the hot plasma/air mixture is convected to the shear layer along the leading edge. From 720 to $860 \mu\text{s}$, the mixture inside the cavity is re-ignited. It is inferred that the radicals and heat from LIP is partially re-circulated into the cavity, which eventually initiates the auto-ignition in the cavity. A similar initial flame development for the LIP ignition at $c-1$ is given in Fig. 4.40. After a LIP ignition at $c-1$, the initial flame quenches at $140 \mu\text{s}$ and it takes a longer time (from 140 to $820 \mu\text{s}$) for the mixture in the cavity to be re-ignited.

Fig. 4.39 CH^* chemiluminescence images after LIP ignition at $a-1$ with $\Phi = 0.30$ [26]

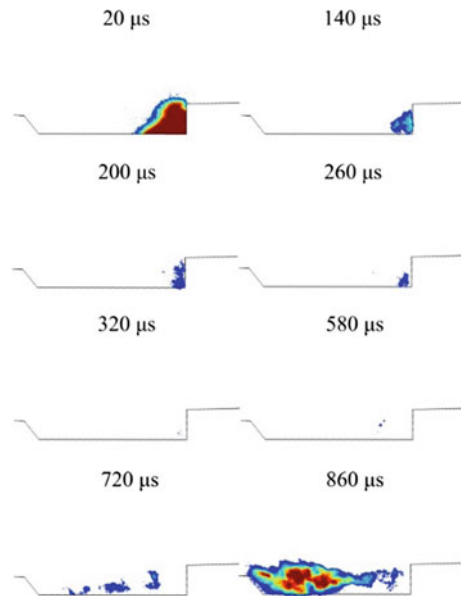


Fig. 4.40 CH* chemiluminescence images after LIP ignition at *c-1* with $\Phi = 0.30$ [26]

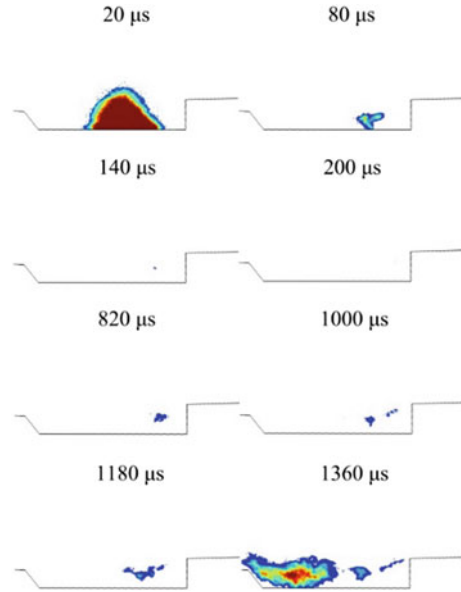
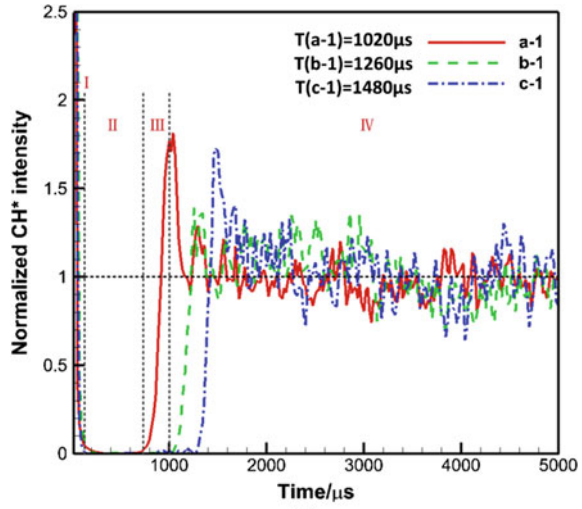


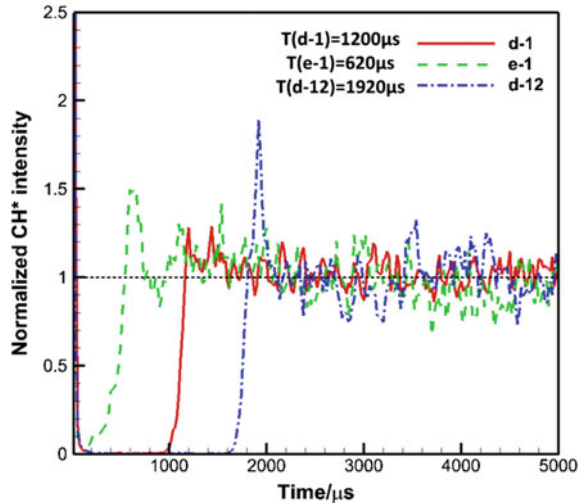
Figure 4.41 shows the integration of intensities over CH* chemiluminescence images obtained in the cases with $\Phi = 0.30$. From Figs. 4.35–4.37 and Figs. 4.39–4.41, it is clear that the ignition process in the cavity at various LIP positions can be summarized as four stages. The first stage is the ‘plasma ignition’ stage (I), during which the residual thermal and plasma effects of the laser are important. The second stage is the ‘plasma quenching’ stage (II), during which the cooling from the ambient cold gas results in quenching of the chemical reactions introduced by the plasma. A lower CH* chemiluminescence signal indicates low chemical reaction rates. The third stage is the ‘re-ignition’ stage (III), during which the residual gas from the LIP initiates auto-ignition of the mixture. This stage can be characterized with the onset of CH* chemiluminescence. The final stage is the ‘stable flame’ stage (IV), during which the ignition process in the cavity has completed and a stable flame has been established in the shear layer.

The ignition time may refer to the time interval from the LIP ignition event to the moment at which the integrated signal of CH* chemiluminescence image reaches its maximum (at the end of stage III). As plotted in Fig. 4.41, the ignition time is sensitive to the LIP ignition positions. The ignition time first increases when the LIP position varies from *a-1* to *c-1*, then decreases when the LIP position changes from *d-1* to *e-1*. Furthermore, the ignition time increases when moving the LIP position vertically from *d-1* to *d-12*. Therefore, *e-1* is preferred as the LIP ignition position since it has the shortest ignition time.

Fig. 4.41 Integrated CH* chemiluminescence against time after LIP ignition at different positions with $\Phi = 0.30$ [26]



(a)



(b)

4.3.2.3 Fluid Flow and Mixing in the Cavity

To further explore the LIP ignition process in the cavity, LES of the mixing process prior to the LIP ignition is carried out. The grid independency analysis adopts two grids: a moderate grid with 11,690,775 cells and a refined grid with 17,536,163 cells. Figure 4.42 plots the wall-pressure distributions from the numerical simulations and experiments when $\Phi = 0.30$. Here, $x = 0$ denotes the combustor inlet. The cavity is located in $x = 410-520$ mm. It can be seen that the numerical results match the experimental data reasonably well, except that around $x = 600$ mm the wall pressure

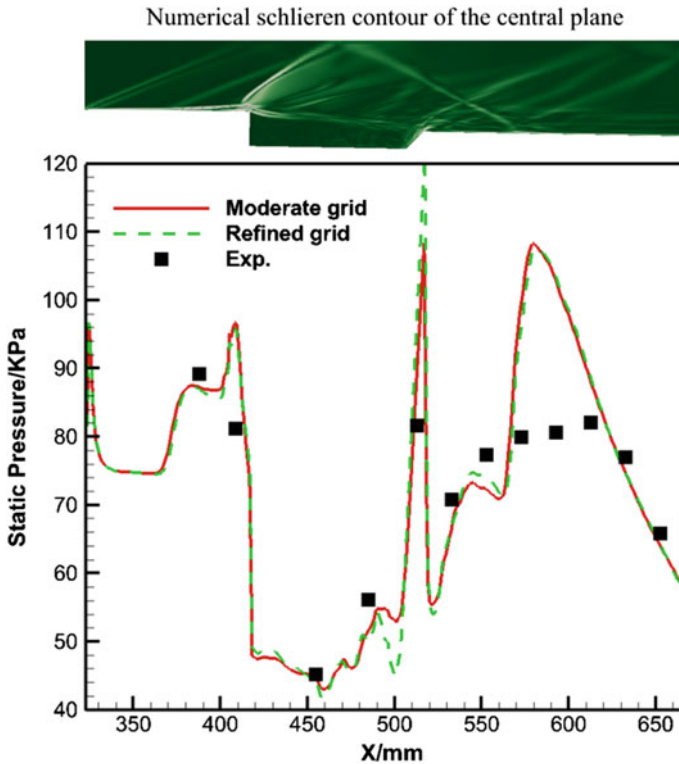


Fig. 4.42 Wall-pressure distribution along the combustor floor with $\Phi = 0.30$ from experiment (Exp.) and LES using two different grids, a moderately fine grid and a refined grid. A two-dimensional distribution of the density gradient (numerical schlieren) is also shown at the top [26]

is overestimated. Additionally, the refined grid leads to only a slight difference in the wall-pressure distribution. Thus the moderate grid with is chosen in the simulation.

There are two sources of errors in the simulations, namely numerical error and systematic error. The numerical error can be caused by the inaccuracy of temporal integration and spatial discretization, the spatial resolution, and the time duration of the numerical simulation to achieve a statistically stationary flow. The systematic error is often caused by the inaccuracy in the physical models such as the turbulent model and the boundary conditions. In the LES presented in this section, the time-averaged flow properties such as wall-pressure distribution shown in Fig. 4.42 are converged. So the numerical error is considered not significant. Considering the boundary-layer separation zone revealed in the numerical schlieren contour around $x = 600$ mm, the discrepancies in Fig. 4.42 are most likely ascribed to the slip wall boundary condition applied to the combustor top wall and the inaccuracy of inflow turbulent boundary conditions. The difference is nevertheless acceptable as the pressure distribution along the wall from the simulations is in a good agreement

with that in the experiments. Based on the comparison of results and other related validation works [10, 11, 22, 32], it can be concluded that the present numerical solver can capture the non-reacting supersonic flow-field successfully.

Figure 4.43 shows the time-averaged local equivalence ratio with isolines of stoichiometric mixture in seven spanwise planes along the streamwise direction. The velocity fields in two representative slices are also plotted. From Figs. 4.43, 4.38 and 4.42, the mixing field and flow structures in the combustor can be understood. The fuel injections generate a pair of roll-up vortices that are convected downstream in the cross flow. Owing to the expansion of the combustor geometry the fuel is directed toward the cavity. A rather uniform distribution of equivalence ratio can be found in the four downstream spanwise planes. There exists a strong shockwave in the leading edge of the cavity, which is deflected at the top wall. Another weaker shockwave is formed at the trailing edge of the cavity.

It is obvious that fuel entrainment depends on the shear layer of the cavity and the recirculation zone structure. As plotted Fig. 4.38, the fuel stream is recirculated into the rearward of the cavity, in accordance with Ref. [36]. The local equivalence ratios in the cavity rearward reveal a fuel-rich environment formed there. We have found in Sect. 4.3.2.2 that a shorter ignition time is obtained when implementing LIP ignition at $e-1$ and $d-1$. Then it is deduced that local fuel-rich environment contributes to successful ignition inside the cavity.

Figure 4.43 reveals that the stoichiometric lines are mainly above the fuel plume and in the outer edge of the shear layer. Inside the cavity, the stoichiometric lines exist in the bottom right corner where the equivalence ratios are low. This local fuel-lean environment agrees well with the discussion about failures of LIP ignition at $a-1$ and $b-1$ when $\Phi = 0.16$.

Figure 4.44 presents the distribution of enstrophy (Ω^2 , where Ω is the magnitude of the vorticity) near the cavity. Enstrophy represents the production of turbulence, and turbulent kinetic energy reflects the fuel/air mixing rate. As shown in Fig. 4.44a, two large-scale fuel-plumes are convected downstream during which the plumes continuously break into smaller fuel-rich pockets. It is observed that the pair of roll-up vortices transports partial fuel into the cavity. The high enstrophy around the fuel plumes denotes strong turbulence and turbulent mixing in the shear layer. As plotted in Figs. 4.43b and 4.45, the enstrophy, scalar dissipation rate and turbulent kinetic energy tend to rise along the streamwise direction. This means as the plumes cross the cavity, the mixing rate increases and then more fuel would be entrained into the cavity, which explains the equivalence ratio distribution in the cavity shown in Figs. 4.38c and 4.43a.

According to the sonic lines plotted in Fig. 4.45, all LIP positions except $d-18$ are situated in the subsonic region. Obviously, the LIP position $d-18$ is inappropriate for ignition owing to the flow conditions. The present results show that LIP ignition site inside the subsonic zones is necessary to achieve a successful ignition in a scramjet combustor. Figure 4.45 also reveals the turbulent conditions in the cavity rearward. The failure at $f-1$ can be seen as a combination of strong dissipation rate and turbulent kinetic energy. Considering the flow direction, the turbulent conditions and the equivalence ratios around $e-1$, it is in favor of the re-ignition stage (stage

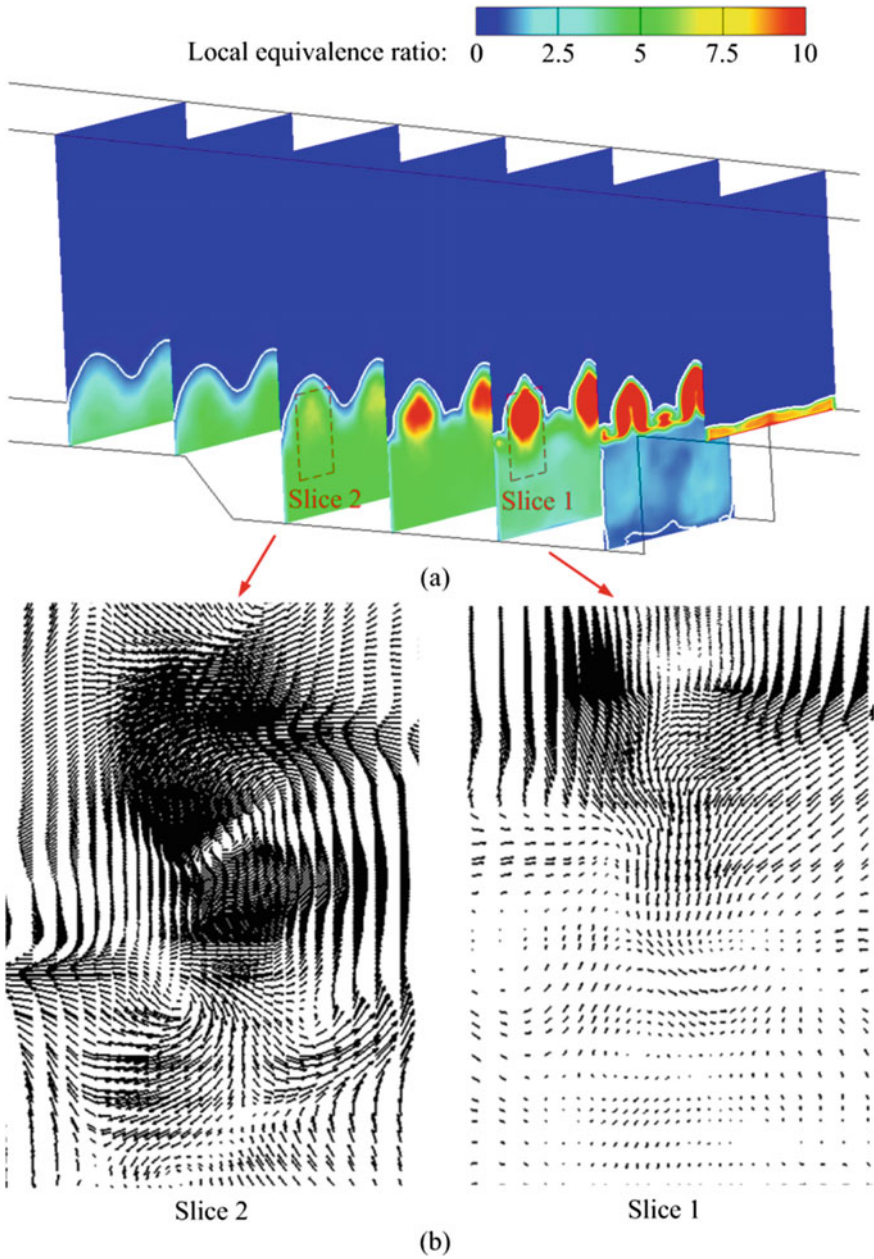


Fig. 4.43 **a** Time-averaged local equivalence ratio distribution and **b** velocity fields in different streamwise planes. The results are from LES with $\Phi = 0.30$ and the moderate grid [26]

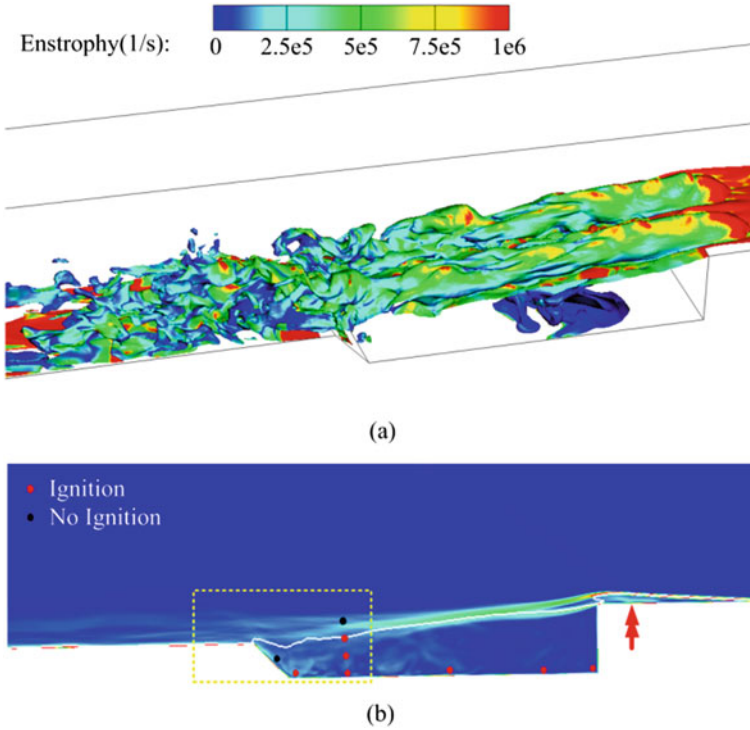


Fig. 4.44 Enstrophy distributions from LES with the moderate grid and $\Phi = 0.30$ [26]. **a** Representative instantaneous iso-surface with ethylene mass fraction being 0.15. **b** Time-averaged enstrophy field with sonic lines in the central plane

III). On the other hand, both the scalar dissipation rate and turbulent kinetic energy are higher at LIP ignition site $f-1$, which will enhance the plasma quenching stage (stage II) and less favorable to re-ignition stage (stage III), and possibly leading to LIP ignition failure.

4.3.3 Ignition Modes

As listed in Table 4.4, four ignition cases were conducted and each case was executed at least five times. In the table, P_i represents the fuel injection pressure and Φ the global equivalence ratio. The cavity fuelling rate is changed by altering the injection pressure. LIP ignitions in all the cases are successful. When the equivalence ratio is less than 0.15, however, successful LIP ignition could not be achieved. The global equivalence ratio in Case 1 is just above the lean ignition limit in the present supersonic combustor.

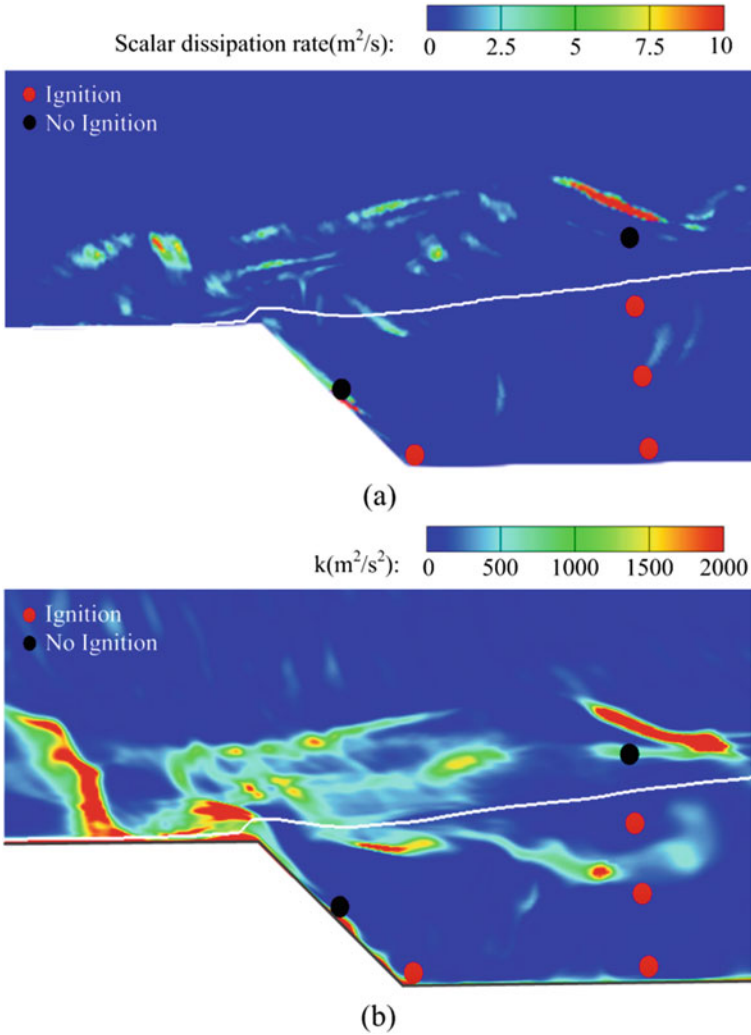


Fig. 4.45 Instantaneous local scalar dissipation rate and turbulent kinetic energy in the rearward of the cavity, obtained from LES with the moderate grid with $\Phi = 0.30$ [26]. **a** Representative instantaneous scalar dissipation rate with sonic lines. **b** Representative instantaneous turbulent kinetic energy with sonic lines

Table 4.4 Experimental arrangements of all test cases

Test case	P_i (MPa)	ϕ	Laser energy (mJ/pulse)
Case 1	0.75	0.15	200
Case 2	1.14	0.23	200
Case 3	1.15	0.23	300
Case 4	2.00	0.40	200

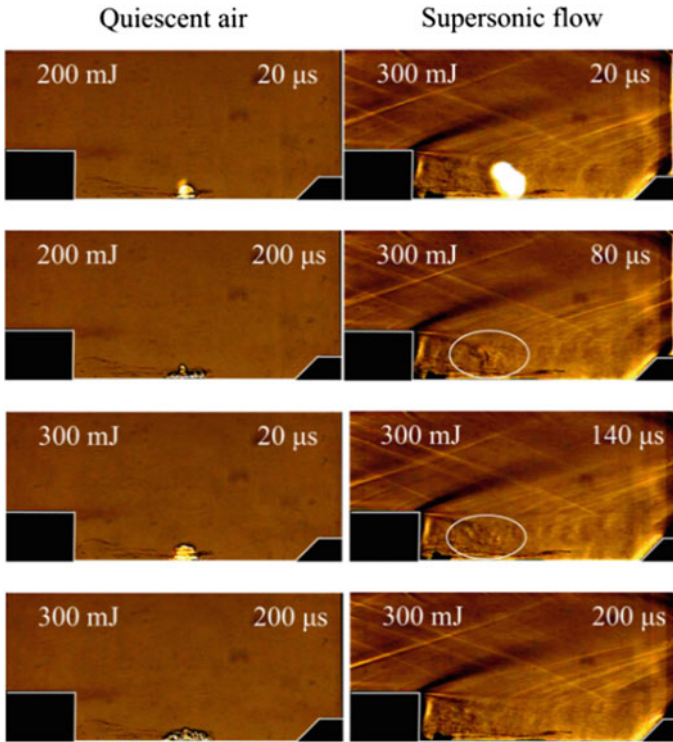


Fig. 4.46 Schlieren images of LIP motions in quiescent (left) and supersonic (right) air flow [28]

Figure 4.46 presents a series of Schlieren images for the laser excitation in quiescent and supersonic air flows. The LIP regions, with noticeable density gradients caused by thermal effects of the LIP, are clearly seen in the images. In the quiescent air flow the thermal region grows as the laser energy increases, which is plotted in the left column. In the supersonic air flow, the LIP region formed by a laser energy of 300 mJ disappears within a time span of 0.2 ms, demonstrating the strong turbulent heat transfer in the cavity. The CH^* has been proved as a good reaction zone marker which could trace regions of flame front and heat release [34]. In addition, the high-temperature product zones can be traced by the OH^* [37]. Figure 4.47 presents consecutive images of CH^* and OH^* chemiluminescence, and the corresponding Schlieren images for case 1. The LIP event begins at $t = 0$ ms.

The transition from LIP excitation to the establishment of a stable flame can be described as two main regimes. The first is the LIP initiation regime shown in Fig. 4.47 when $t < 0.8$ ms. The initial signals of CH^* and OH^* chemiluminescence are from the LIP excitation. Between $t = 0.1$ ms and $t = 0.8$ ms, the chemiluminescence intensities decrease rapidly because of the turbulent heat transfer shown in Fig. 4.46.

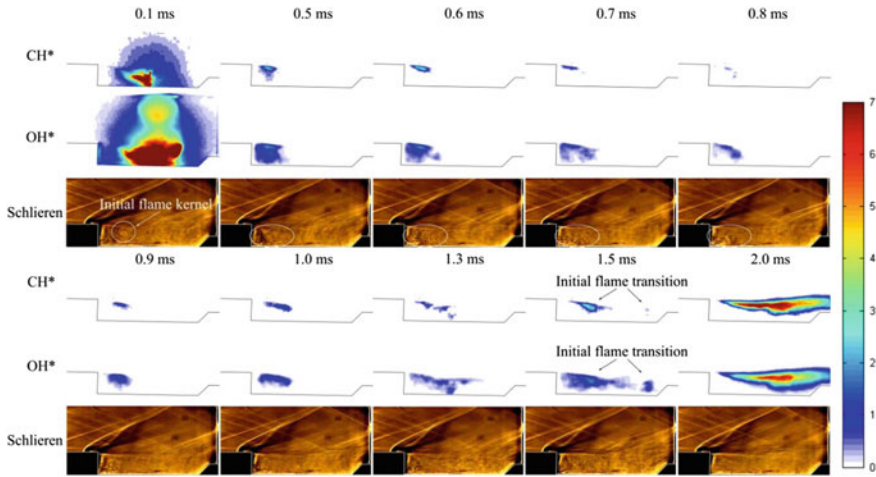


Fig. 4.47 Simultaneous CH*/OH* chemiluminescence and Schlieren images during the LIP ignition process for case 1 [28]

The second is the transient ignition reaction regime. After $t = 0.8$ ms, the chemiluminescence intensities start to increase, denoting the onset of the ignition. Before $t = 2$ ms, the CH* mainly lies in a narrow region in the shear layer near the front wall of the cavity. The OH* signals are found in a larger area than the CH*, since the life time of OH* is much longer in reactive flows [38]. It appears that the thermal effect of the LIP provides favorable thermal and chemical environment for the ignition process. When a stable flame is established at $t = 2.0$ ms, the CH* and OH* regions overlap each other with the OH* distribution slightly deeper into the cavity.

Figure 4.48 shows the CH* and OH* chemiluminescence images during the LIP ignition process for case 4. The two-regime ignition process discussed earlier for case 1 can be identified in the figure as well. It takes a shorter time to establish a stable flame due to the higher equivalence ratio in case 4 than in case 1. The first regime (the LIP initiation) ends at $t = 0.4$ ms, during which the intensities of CH* and OH* chemiluminescence attenuate because of the turbulent heat transfer. The onset of the ignition can be observed at $t = 0.5$ ms when the chemiluminescence starts to increase. Compared with case 1, in case 4 the transient ignition reaction regime is

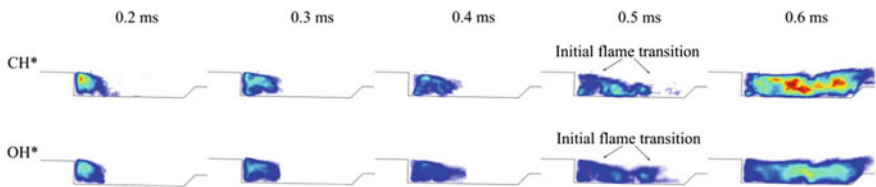


Fig. 4.48 Simultaneous CH*/OH* chemiluminescence images of the LIP ignition process for case 4 [28]

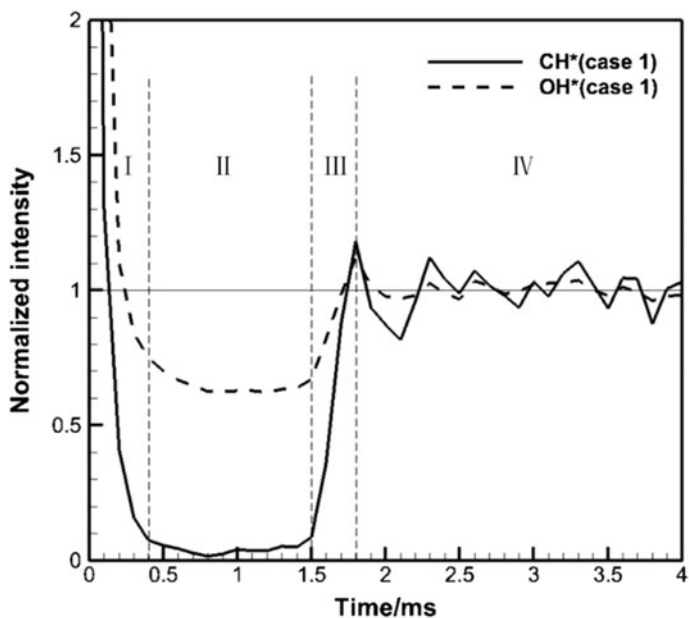
shorter and the CH* region is much wider. The CH* and OH* regions overlap rather well in case 4. It is clear that the equivalence ratio has a significant impact on the ignition process in the cavity-based supersonic combustor.

In order to characterize the two-regime LIP ignition process of the four cases, the intensities of CH* and OH* chemiluminescence images are integrated in each frame and the results are shown in Fig. 4.49. The integrated intensities in each case are normalized by its mean intensity at the stable flame period [39]. As discussed in Fig. 4.41, the LIP-assisted cavity ignition process is classified into four stages, involving 'initial plasma ignition', 'plasma quenching', 're-ignition' and 'stable flame'. It is obvious that the two-regime LIP ignition process discussed in Figs. 4.47 and 4.48 is consistent with the four stages. The first laser initiation regime corresponds to stage I and the first part of stage II, whereas the transient ignition reaction regime relates to the later part of stage II and stage III. However, stages II and III in cases 3 and 4 are much shorter than in cases 1 and 2, because case 3 has a higher laser energy and case 4 a larger fuelling rate (equivalence ratio).

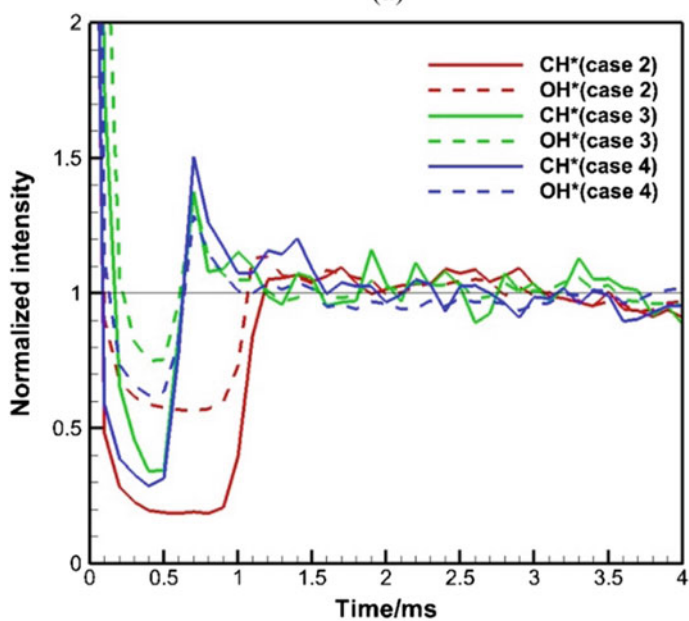
The impacts of the fuelling rate and the laser energy on the cavity ignition process can be explained using the two-regime ignition mechanism. With a low fuelling rate (e.g., the global equivalence ratio is lower than 0.15), the heat release and radicals [40] formed from the LIP initiation regime are not sufficient to survive in the turbulent heat transfer, which results in the ignition failure. As the fuelling rate increases, the heat release in the upstream half cavity is larger, and then the reactions would not be quenched, the mixture in the rearward of the cavity therefore being ignited. With further increase in the fuelling rate or the laser energy, the onset of the ignition in the cavity rearward becomes faster and a stable flame can be established in a shorter time.

Figure 4.50 is plotted to further characterize the ignition process in the cavity. For each case the CH* chemiluminescence intensities in a frame are integrated respectively in the half cavity (from the front wall to the middle of the cavity) and the whole cavity. Then the integrated intensities are normalized by the time-averaged intensity of the whole cavity. The two normalized intensities are nearly the same during the LIP initiation regime, since the hot LIP gas is mainly found in the upstream half of the cavity. In the final stable flame stage, nevertheless, the normalized intensity in the upstream half of the cavity is much lower, showing that the chemical reactions chiefly occur in the downstream half.

Inspecting the differences of chemiluminescence images among diverse cases from Figs. 4.47, 4.48 and 4.50, it is evident that for the LIP ignition process there are two modes. In the weak ignition mode (case 1), the initial flame kernel anchored near the cavity shear layer is too weak to directly ignite the fuel in the rearward of the cavity. As in the whole cavity the environment is fuel-lean, the initial flame transits gradually from the upstream cavity to the rearward. This mode exists in the fuel-lean cavity. In the intense ignition model (case 4), a strong flame is formed immediately after the laser excitation owing to the favorable environment. Then following the recirculation flow the initial flame spreads quickly to the upstream cavity corner.



(a)



(b)

Fig. 4.49 Normalized CH^* and OH^* chemiluminescence intensity against time for different cases [28]. Each normalized intensity is a time-averaged result of repeated experiments for the same case

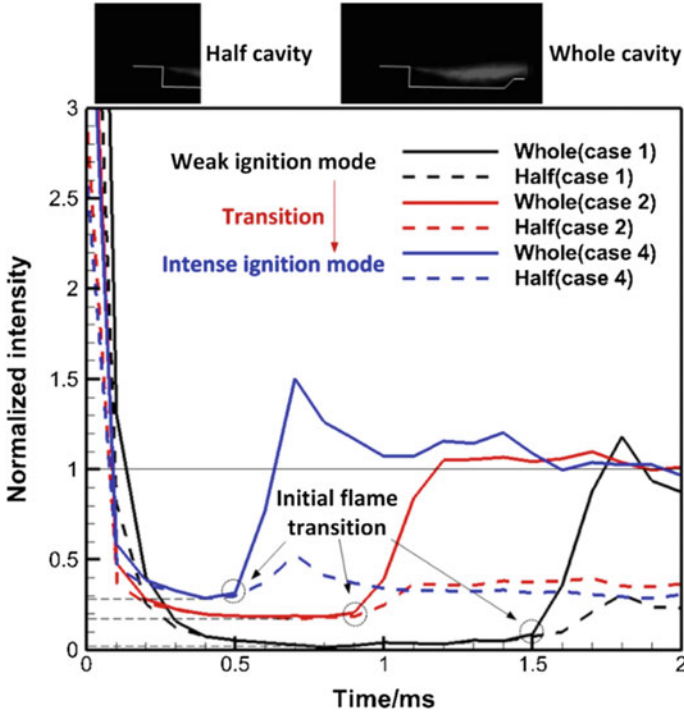
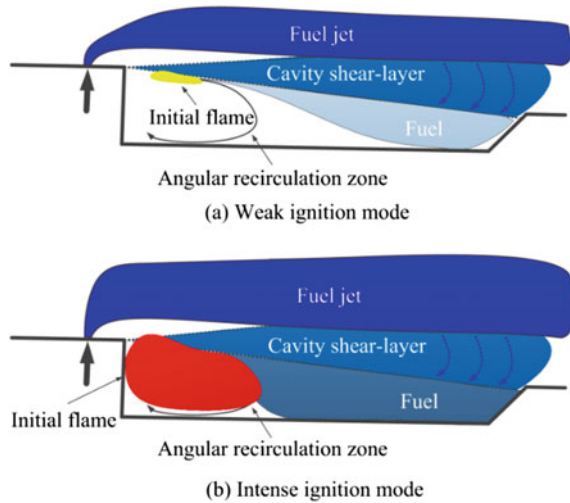


Fig. 4.50 Normalized CH* chemiluminescence intensity against time for different ignition modes [28]

Since the initial flame is robust enough to ignite the fuel in the rearward of the cavity, it only takes a rather short residence time before a stable flame is achieved. It is observed that there also exist transitional behaviors of the initial flame between the weak and the intense ignition modes, e.g. cases 2 and 3.

Figure 4.51 illustrates the schematic of the flowfield, fuel/air mixing and reaction zone structure based on the previous works in Refs. [10, 41, 42]. It is inferred that the ignition process is mainly assisted by the cavity recirculation zone in the weak ignition mode. But in the intense ignition mode, the initial flame directly leads the ignition process. For the transition between the two modes, the ignition process is dominated both by the cavity recirculation zone and the initial flame. It should be noted that in the intense mode the occurrence of the cavity recirculation zone is still favorable, because it also provides the flow field and mixing environments friendly for ignition.

Fig. 4.51 Schematic of the reaction zone structure of the strong and weak ignition modes [28]



4.4 Auto-Ignition Effects

As the stagnation temperature increases, the effects of auto-ignition on combustion characteristics in the cavity-based scramjet combustor need more consideration. In this section, hydrogen was transversely injected upstream of the cavity. The effects of auto-ignition were investigated experimentally under stagnation temperature of 1400 K and 1600 K, respectively imitating the flight Mach numbers 5.5 and 6.

4.4.1 Experimental Setup

The experiments were carried out in a recently developed direct-connect test facility. Pure ethanol and oxygen were burned continuously to heat the air, providing a vitiated air stream of Mach 2.52 with the stagnation temperatures of 1400 K and 1600 K. The fuel injection last 1.5 s, and during this period the fueling rate was steady according to the mass flowmeter. Table 4.5 reports the operation conditions.

Schematic of the test section is plotted in Fig. 4.52. The combustor had a width of 50 mm and a height of 40 mm. Installed on the bottom wall was a cavity with the depth $D = 8$ mm, the length-to-depth ratio $L/D = 7$ and the rear wall angle $A = 45^\circ$. A spark ignition plug was mounted 10-mm downstream of the leading edge of the cavity. An injector with an orifice diameter of 2 mm was fixed 160-mm upstream of the cavity. High-speed imaging of flame luminosity and schlieren were introduced in the test section. The frame rate was set to 15000 frame/s with an exposure time of 0.067 ms. The pressure distribution along the centrelines of the top and bottom walls in the test section was measured by a pressure scanner with a 100-Hz acquisition

Table 4.5 Experimental conditions

Parameter		Scheme 1	Scheme 2
Air	T_0 , K	1600	1400
	P_0 , MPa	1.65	1.55
	Ma	2.52	2.52
	Y_{O_2} , %	23.38	23.38
	Y_{H_2O} , %	7.13	5.92
	Y_{CO_2} , %	11.67	9.68
	Y_{N_2} , %	57.82	61.0
H ₂	P_{0jet} , MPa	3.5–5.0	
	Equivalence ratio (Φ)	0.22–0.32	
	Y_{H_2} , %	99.5–99.8	
	Y_{other} , %	0.2–0.5	

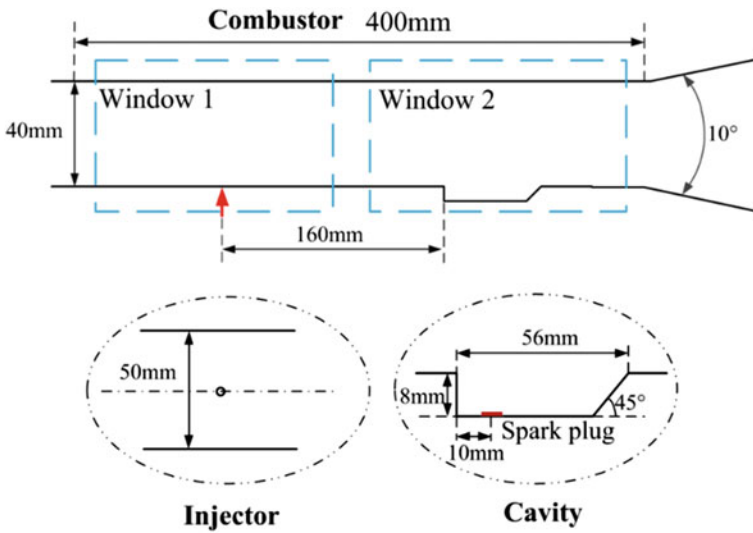
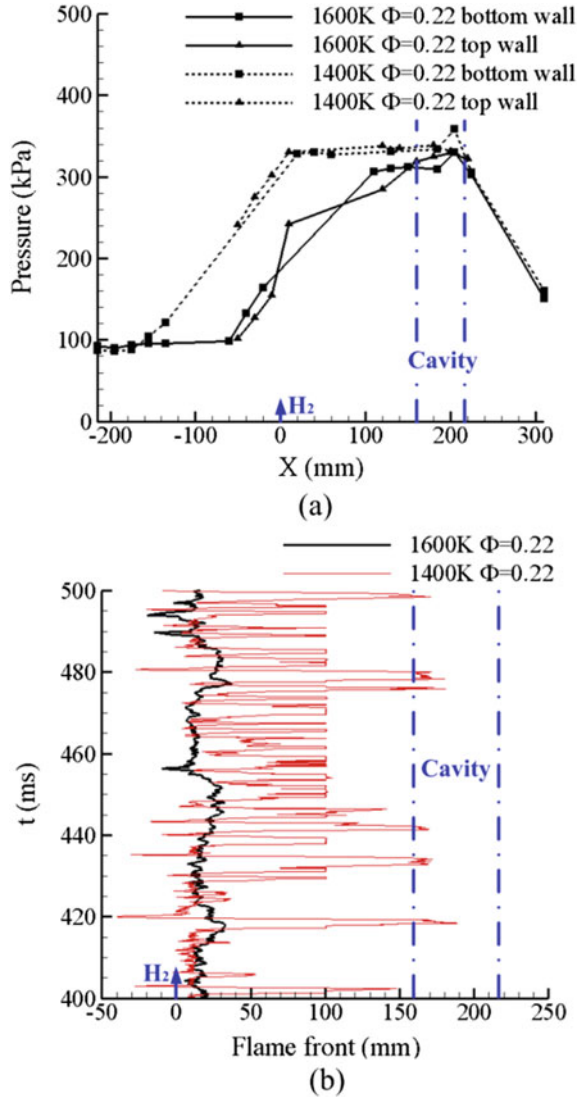


Fig. 4.52 Schematic of the test section (top) and zoomed views around the injector and the cavity (bottom) [43]. The red arrow denotes the fuel injection location

frequency and 0.25% full scale accuracy. More details about the experimental facility can be obtained from the previous works [12, 44].

There is a concern on the OH concentration in the vitiated air produced by the ethanol/O₂ combustion, since OH radicals have a significant role in the H₂/O₂ auto-ignition. The OH-PLIF results, however, showed that the OH concentration was actually low and can be negligible, as discussed in Ref. [45].

Fig. 4.53 **a** Comparison of the time-averaged pressure along the centerlines of bottom wall and top wall in the combustor, and **b** the dynamics of the flame front from 400 to 500 ms after the fuel injection begins [43]



4.4.2 Auto-Ignition in the Ignition Process

Table 4.6 lists the ignition schemes and combustion stabilization modes at the equivalence ratios from 0.22 to 0.32 under the stagnation temperature T_0 of 1400 K and 1600 K, respectively. When $T_0 = 1400$ K, the fuel could be ignited successfully only by the spark ignition. When $T_0 = 1600$ K, however, auto-ignition was achieved in the combustor. Obviously, auto-ignition would be more significant with increase of

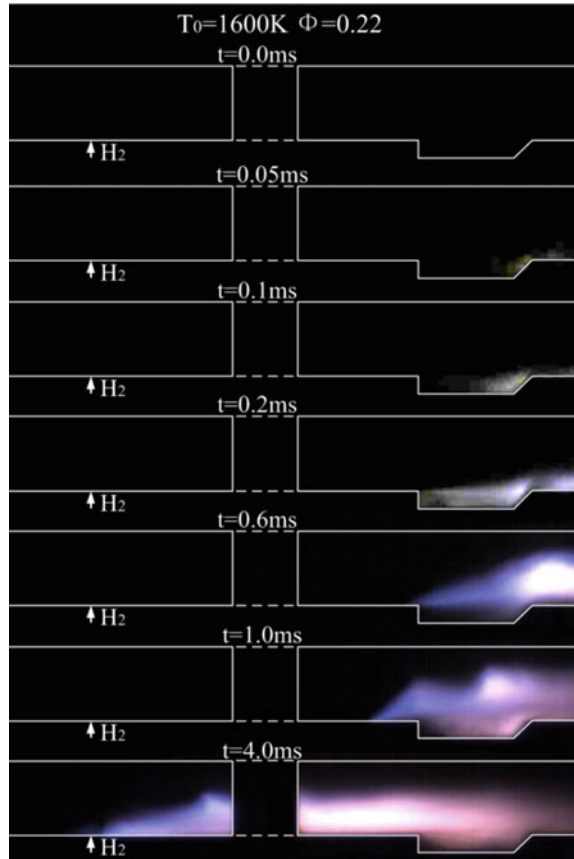
Table 4.6 Ignition schemes and combustion stabilization modes

T_0 , K	P_{0jet} , MPa	Φ	Ignition scheme	Combustion stabilization mode
1400	3.5–5.0	0.22–0.32	Spark	Jet-wake stabilized mode combined with cavity stabilized mode
1600	3.5–5.0	0.22–0.32	Auto-ignition	Jet-wake stabilized mode

the stagnation temperature. It provides some new ideas for designing the ignition schemes for scramjet under high flight Mach numbers.

As reported in Table 4.6, the jet-wake stabilized mode is obtained under both stagnation temperatures. Figure 4.54a shows the time-averaged pressures along the combustor walls; Fig. 4.54b presents the dynamics of flame fronts against times. The pressure when $T_0 = 1600$ K is lower from $X = 0$ mm to $X = 100$ mm than in $T_0 = 1400$ K, which suggests that the time-averaged flame in the jet is less intense in the former. On the contrary, the flame front is more stable in the jet wake with

Fig. 4.54 High-speed flame luminosity images in the initial phase of the combustion with auto-ignition [43]



$T_0 = 1600$ K. With $T_0 = 1400$ K, the flame front fluctuates between $X = -50$ mm (upstream of the injector) and $X = 180$ mm (in the cavity). It is then concluded that the combustion is accompanied by intermittent blow-off and restabilization in the jet wake. During the unsteady process an interesting phenomenon was repeatedly observed that an individual flame appeared in the jet upstream of the original flame in the cavity. This phenomenon took place under different equivalence ratios from 0.22 to 0.32.

Figure 4.54 presents the instantaneous flame luminosity images with $T_0 = 1600$ K and $\Phi = 0.22$. The initial flame core initially appears close to the rear wall of the cavity because of auto-ignition. Then the flame core develops in the recirculation zone of the cavity. Following that the jet around the cavity is ignited, and then the flame propagates upstream. Finally, a jet-wake stabilized flame is formed, as shown in the bottom subfigure.

Figure 4.55 shows the typical loop from blow-off to restabilization under the stagnation temperature of 1400 K. The loop begins at $t = 477$ ms and ends at $t = 481$ ms, as plotted in Fig. 4.53b. As shown in Fig. 4.55, the flame is first stabilized in the jet wake with the flame front close to the injector. The precombustion shock train is located upstream of the injector. Then, the flame is blown downstream along with the

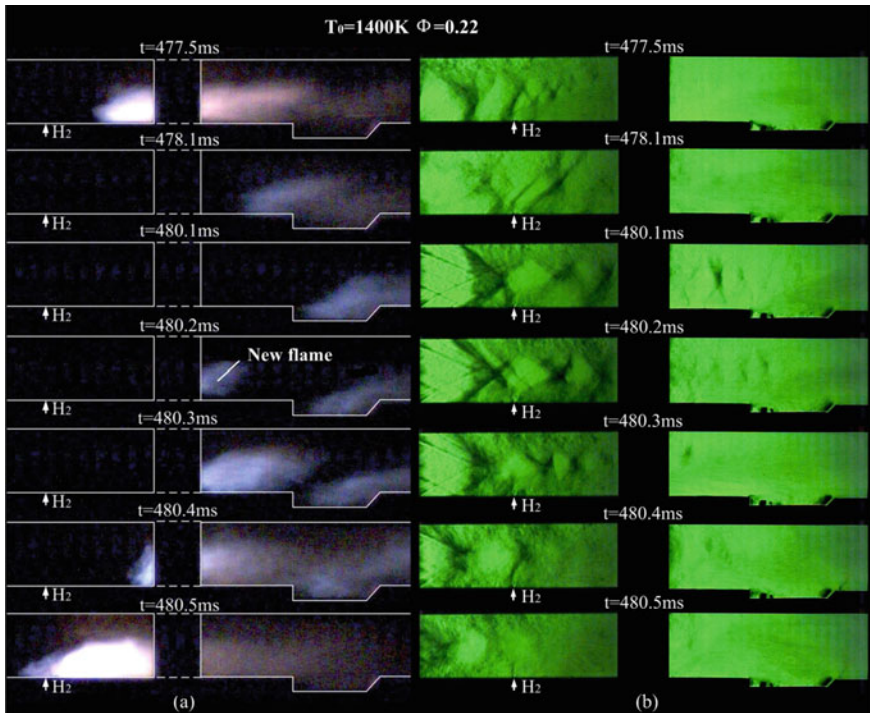


Fig. 4.55 Typical loop from blow-off to restabilization with $T_0 = 1400$ K [43]. **a** Instantaneous high-speed flame luminosity images. **b** Simultaneously instantaneous high speed schlieren images

shock train. When the weak flame reaches the cavity, the shock train remains upstream of the cavity, compressing the mixed gas and increasing the static temperature. At $t = 480.1$ ms, there exists no flame observed in the jet wake and the flame is completely stabilized in the shear layer of the cavity. At $t = 480.2$ ms, a new flame core suddenly occurs and then develops into an individual flame in the upstream of the cavity. The new flame alters the shock structures and then combines with the original cavity-stabilized flame. The combined flame further propagates upstream, eventually the flame being re-stabilized in the jet wake.

Figure 4.56a shows dynamics of the flame front in the typical loop from blow-off to restabilization. The time interval between adjacent subfigures is 0.067 ms whereby the flame-front-propagation speed is calculated, as plotted in Fig. 4.56b. At $t = 480.1$ ms when the new flame appears, the instantaneous speed would be over 1000 m/s if we assume that the new flame is ascribed to the flame propagation from the cavity. This flame speed is far beyond the turbulent flame propagation limits. Therefore, the new flame is caused by auto-ignition. The different flame behaviors and flame-stabilized modes with $T_0 = 1400$ K and $T_0 = 1600$ K demonstrate the auto-ignition has significant influences on ignition process and combustion stabilization, especially when the stagnation temperature is high.

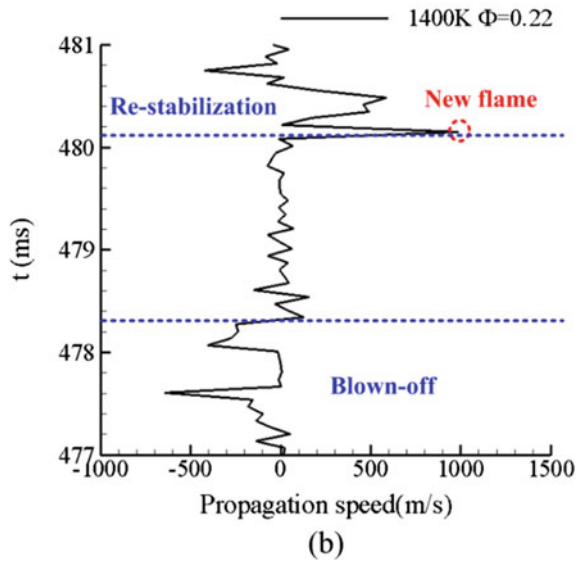
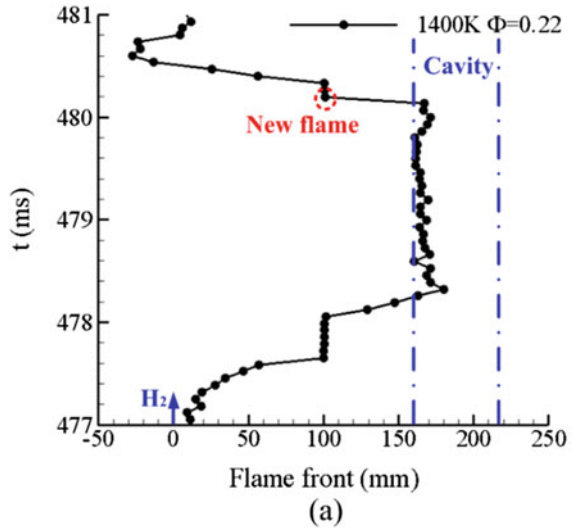
4.5 Summary

Cavities are often used in practical scramjets owing to their minimal system complexity, small total pressure losses and the good performance in flame holding. The cavities could hold the flame because they provide subsonic regions where recirculation zones form and successively furnish the core flow with heat and radicals vital for combustion. Considering the inflow conditions, ignition of cavity-based scramjets aims to initialize the combustion in the cavities, since in other places the turbulent dissipation is usually too severe to maintain the initial flame.

Ignition is to inject a certain amount of energy into the fuel/air mixture, with the purpose of triggering oxidation reactions which could further propagate in the combustor. Variables concerned in the energy injection process includes how to inject energy, the ignition energy amount, the ignition position, and the inflow conditions. These variables and their influences are usually the intents of studies about cavity ignition. Since cavity ignition is intrinsically and partially stochastic, it is of significance that the dynamics during the ignition process. Both experimental and numerical investigations show that the cavity ignition process is a strong coupling of subsonic flow, supersonic flow, heat and molecular transfer, and chemical reactions.

There are various ignition techniques corresponding to different ways to inject the ignition energy. Spark ignition, piloted ignition, GAD ignition and LIP ignition are introduced. Except for the piloted ignition, the other three techniques are all based on plasmas. In the spark ignition and the LIP ignition, equilibrium plasmas are produced, thus the mixture being ignited mainly by the heat effects of the plasmas. Nonetheless, the GAD generates nonequilibrium plasmas which could selectively stimulate

Fig. 4.56 **a** The dynamic of the flame front in the typical loop from blow-off to restabilization; **b** the propagation speed of the flame front during the loop [43]



nonequilibrium chemical reactions important for the ignition process. Instead of plasmas, the piloted ignition is based on the combustion of piloted fuel (often Hydrogen) and air. Further, the generated heat and radicals are distributed in both in and out the cavity, very different from the other ignition techniques. Among the four techniques, the piloted ignition could provide a large amount of ignition energy just by increasing the mass flow rate of piloted fuel; however, the LIP ignition is most suitable for studying the flame kernel formation because this technique has the highest accuracy in manipulating the ignition energy, position and timing.

After the ignition energy is injected into the cavity at a specific region and initial chemical reactions are triggered there, the flame kernel formation is primarily dominated by confrontation between the chemical reactions and the turbulent dissipation. A success cavity ignition requires that the chemical reactions in the cavity produce enough heat and radicals which ignite the fuel/air mixture in the shear layer. According to the flow direction and the fuel distribution in the cavity, the ignition position matters. Ignition near the rear wall of the cavity is preferred: first the equivalence ratio is high there; second the hot plasmas have enough time to fully contact with the fuel/air mixture in the cavity. If the ignition position is close to the front wall, the hot plasma would be quickly transferred into the shear layer and then quenched. Then the reduced heat release and radical generation might fail to ignite the fuel/air mixture in the shear layer. Increase of the ignition energy enhances the chemical reactions in the cavity and thus promotes the cavity ignition.

The whole ignition process can be divided into four stages. The first stage begins with the ignition event and ends when the plasmas quench, meaning that the energy in the plasmas is transferred to the mixtures in the cavity. The second stage corresponds to an accumulation of heat and radical in the cavity. After a period of time the fuel/air mixture in the cavity would start to combust and the mixture in the shear layer would be ignited, which is the third stage. In the final stage the flame is mainly in the shear layer, and partial high-temperature products are transported from the rear wall of the cavity to the front wall, and finally into the shear layer. As duration of the second stage decreases, the cavity ignition becomes stronger.

It is noteworthy that the fuel/air mixture might auto-ignite. If the stagnation temperature is improved to a critical value, there is no need for forced ignition. The oxidation reactions happen spontaneously when the fuel/air mixture passes through the isolator and the combustor, and then the heat and radicals accumulate in the cavity. After some accumulation there would be auto-ignition in the cavity. Slightly lowering the stagnation temperature and utilizing forced ignition in the cavity, the auto-ignition could occur upstream of the cavity. A possible position of auto-ignition is the downstream separation zone induced by the fuel jet. This kind of auto-ignition is able to bring about combustion unsteadiness.

References

1. Sun, M., Gong, C., Zhang, S., Liang, J., Liu, W., & Wang, Z. (2012). Spark ignition process in a scramjet combustor fueled by hydrogen and equipped with multi-cavities at Mach 4 flight condition. *Experimental Thermal and Fluid Science*, 43, 90–96.
2. Xi, W., Wang, Z., Sun, M., Liu, W., & Li, Q. (2014). Experimental investigation of ignition transient phase in model supersonic combustor. *Journal of Aerospace Engineering*, 27, 1–9.
3. Feng, R., Li, J., Wu, Y., Zhu, J., Song, X., & Li, X. (2018). Experimental investigation on gliding arc discharge plasma ignition and flame stabilization in scramjet combustor. *Aerospace Science and Technology*, 79, 145–153.

4. Huang, S., Wu, Y., Song, H., Zhu, J., Zhang, Z., Song, X., et al. (2018). Experimental investigation of multichannel plasma igniter in a supersonic model combustor. *Experimental Thermal and Fluid Science*, 99, 315–323.
5. Phuoc, T. X. (2006). Laser-induced spark ignition fundamental and applications. *Optics and Lasers in Engineering*, 44, 351–397.
6. Li, X., Liu, W., Pan, Y., Yang, L., & An, B. (2017). Experimental investigation on laser-induced plasma ignition of hydrocarbon fuel in scramjet engine at takeover flight conditions. *Acta Astronautica*, 138, 79–84.
7. Li, X., Liu, W., Pan, Y., Yang, L., An, B., & Zhu, J. (2018). Characterization of ignition transient processes in kerosene-fueled model scramjet engine by dual-pulse laser-induced plasma. *Acta Astronautica*, 144, 23–29.
8. An, B., Wang, Z., Yang, L., Li, X., & Zhu, J. (2017). Experimental investigation on the impacts of ignition energy and position on ignition processes in supersonic flows by laser induced plasma. *Acta Astronautica*, 137, 444–449.
9. Cai, Z., Wang, Z., Sun, M., Wang, H., & Liang, J. (2014). Investigation of the spark ignition enhancement in a supersonic flow. *Modern Physics Letters B*, 28, 1–8.
10. Cai, Z., Liu, X., Gong, C., Sun, M., Wang, Z., & Bai, X.-S. (2016). Large Eddy simulation of the fuel transport and mixing process in a scramjet combustor with rearwall-expansion cavity. *Acta Astronautica*, 126, 375–381.
11. Cai, Z., Wang, Z., Sun, M., Bai, X.-S. (2016). Effect of combustor geometry and fuel injection scheme on the combustion process in a supersonic flow. *Acta Astronautica*, 129, 44–51.
12. Cai, Z., Yang, Y., Sun, M., & Wang, Z. (2016). Experimental investigation on ignition schemes of a supersonic combustor with the rearwall-expansion cavity. *Acta Astronautica*, 123, 181–187.
13. Cai, Z., Zhu, J., Sun, M., & Wang, Z. (2018). Spark-enhanced ignition and flame stabilization in an ethylene-fueled scramjet combustor with a rear-wall-expansion geometry. *Experimental Thermal and Fluid Science*, 92, 306–313.
14. Cai, Z., Zhu, X., Sun, M., Wang, Z. (2018). Experimental study on the combustion process in a scramjet combustor with a rear-wall-expansion geometry. *Journal of Aerospace Engineering*, 31(5), 04018077.
15. Yang, Y., Wang, Z., Sun, M., Wang, H., & Li, L. (2015). Numerical and experimental study on flame structure characteristics in a supersonic combustor with dual-cavity. *Acta Astronautica*, 117, 376–389.
16. Jiang, G., & Shu, C. W. (1996). Efficient implementation of weighted ENO schemes. *Journal of Computational Physics*, 126, 917–923.
17. Wang, H., Qin, N., Sun, M., & Wang, Z. (2012). A dynamic pressure-sink method for improving large eddy simulation and hybrid Reynolds-averaged Navier-Stokes/large eddy simulation of wall-bounded flows. *Proceedings of the Institution of Mechanical Engineers, Part G: Journal of Aerospace Engineering*, 226, 1107–1120.
18. Jachimowski, C. J. (1988). An analytical study of the hydrogen-air reaction mechanism with application to scramjet combustion, NASA Technical Paper 2791.
19. Wang, H., Qin, N., Sun, M., Wu, H., & Wang, Z. (2011). A hybrid LES (Large Eddy Simulation)/assumed sub-grid PDF (Probability Density Function) model for supersonic turbulent combustion. *Science China Technological Sciences*, 54, 2694–2707.
20. Wang, H., Wang, Z., Sun, M., & Qin, N. (2013). Combustion characteristics in a supersonic combustor with hydrogen injection upstream of cavity flameholder. *Proceedings of the Combustion Institute*, 34, 2073–2082.
21. Wang, H., Wang, Z., Sun, M., & Qin, N. (2015). Large eddy simulation of a hydrogen-fueled scramjet combustor with dual cavity. *Acta Astronautica*, 108, 119–128.
22. Wang, Z., Cai, Z., Sun, M., Wang, H., & Zhang, Y. (2016). Large Eddy simulation of the flame stabilization process in a scramjet combustor with rearwall-expansion cavity. *International Journal of Hydrogen Energy*, 41, 19278–19288.
23. Kouchi, T., Masuya, G., Mitani, T., & Tomioka, S. (2012). Mechanism and control of combustion-mode transition in a scramjet engine. *Journal of Propulsion and Power*, 28, 106–112.

24. Wang, Z., Sun, M., Wang, H., Yu, J., Liang, J., & Zhuang, F. (2015). Mixing-related low frequency oscillation of combustion in an ethylene-fueled supersonic combustor. *Proceedings of the Combustion Institute*, 35, 2137–2144.
25. Chong, D., Hu, M., Chen, W., Wang, J., Liu, J., & Yan, J. (2014). Experimental and numerical analysis of supersonic air ejector. *Applied Energy*, 130, 679–684.
26. Cai, Z., Zhu, J., Sun, M., Wang, Z., & Bai, X.-S. (2018). Laser-induced plasma ignition in a cavity-based scramjet combustor. *AIAA Journal*, 56, 4884–4892.
27. Gao, T., Liang, J., Sun, M., & Zhao, Y. (2017). Analysis of separation modes variation in a scramjet combustor with single-side expansion. *AIAA Journal*, 55, 1307–1317.
28. Cai, Z., Zhu, J., Sun, M., Wang, Z., & Bai, X.-S. (2018). Ignition processes and modes excited by laser-induced plasma in a cavity-based supersonic combustor. *Applied Energy*, 228, 1777–1782.
29. Geerts, J. S., & Yu, K. H. (2016). Shock train/boundary-layer interaction in rectangular isolators. *AIAA Journal*, 54, 3450–3464.
30. Geerts, J. S., & Yu, K. H. (2017). Systematic application of background-oriented schlieren for isolator shock train visualization. *AIAA Journal*, 55, 1105–1117.
31. Greenshields, C. J., Weller, H. G., Gasparini, L., & Reese, J. M. (2010). Implementation of semi-discrete, non-staggered central schemes in a colocated, polyhedral, finite volume framework, for high-speed viscous flow. *International Journal for Numerical Methods in Fluids*, 63, 1–21.
32. Cai, Z., Wang, Z., Sun, M., Bai, X.-S. (2017). Large Eddy simulation of the flame propagation process in an ethylene fueled scramjet combustor in a supersonic flow. In *21st AIAA International Space Planes and Hypersonics Technologies Conference* (pp. 2017–2148). Xiamen, China: AIAA.
33. Cai, Z., Zhu, X., Sun, M., & Wang, Z. (2017). Experiments on flame stabilization in a scramjet combustor with a rear-wall-expansion cavity. *International Journal of Hydrogen Energy*, 42, 26752–26761.
34. Allison, P. M., Frederickson, K., Kirik, J. W., Rockwell, R. D., Lempert, W. R., & Sutton, J. A. (2017). Investigation of supersonic combustion dynamics via 50 kHz CH chemiluminescence imaging. *Proceedings of the Combustion Institute*, 36, 2849–2856.
35. Zhang, S., Wang, X., He, M., Jiang, Y., Zhang, B., Hang, W., et al. (2014). Laser-induced plasma temperature. *Spectrochimica Acta Part B*, 97, 13–33.
36. Wang, H., Li, P., Sun, M., & Wei, J. (2017). Entrainment characteristics of cavity shear layers in supersonic flow. *Acta Astronautica*, 137, 214–221.
37. Wang, H., Wang, Z., Sun, M., & Wu, H. (2013). Combustion modes of hydrogen jet combustion in a cavity-based supersonic combustor. *International Journal of Hydrogen Energy*, 38, 12078–12089.
38. Rasmussen, C. C., Dhanuka, S. K., & Driscoll, J. F. (2007). Visualization of flameholding mechanisms in a supersonic combustor using PLIF. *Proceedings of the Combustion Institute*, 31, 2505–2512.
39. Ombrello, T. M., Carter, C. D., Tamb, C.-J., & Hsueh, K.-Y. (2015). Cavity ignition in supersonic flow by spark discharge and pulse detonation. *Proceedings of the Combustion Institute*, 35, 2101–2108.
40. Brieschenk, S., O’Byrne, S., & Kleine, H. (2013). Laser-induced plasma ignition studies in a model scramjet engine. *Combustion and Flame*, 160, 145–148.
41. Gruber, M. R., Donbar, J. M., Carter, C. D., & Hsu, K.-Y. (2004). Mixing and combustion studies using cavity-based flameholders in a supersonic flow. *Journal of Propulsion and Power*, 20, 769–778.
42. Sun, M., Zhong, Z., Liang, J., & Wang, Z. (2014). Experimental investigation of supersonic model combustor with distributed injection of supercritical kerosene. *Journal of Propulsion and Power*, 30, 1537–1542.
43. Wang, Y., Wang, Z., Sun, M., & Wang, H. (2018). Effects of auto-ignition on combustion characteristics in a hydrogen-fueled dual-mode scramjet combustor. *Acta Astronautica*, 153, 154–158.

44. Sun, M. B., Cui, X. D., Wang, H. B., & Bychkov, B. V. (2015). Flame flashback in a supersonic combustor fueled by ethylene with cavity flameholder. *Journal of Propulsion and Power*, *31*, 976–980.
45. Wang, H. B., Wang, Z. G., & Sun, M. B. (2013). Experimental study of oscillations in a scramjet combustor with cavity flameholders. *Experimental Thermal and Fluid Science*, *45*, 259–263.